We are IntechOpen,
the world's leading publisher of
Open Access books
Built by scientists, for scientists

6,900
Open access books available

185,000
International authors and editors

200M
Downloads

154
Countries delivered to

Our authors are among the

TOP 1%
most cited scientists

12.2%
Contributors from top 500 universities

CLARIVATE ANALYTICS
BOOK CITATION INDEX
INDEXED

WEB OF SCIENCE™

Selection of our books indexed in the Book Citation Index
in Web of Science™ Core Collection (BKCI)

Interested in publishing with us?
Contact book.department@intechopen.com

Numbers displayed above are based on latest data collected.
For more information visit www.intechopen.com

Ion Beams for Materials Analysis: Conventional and Advanced Approaches

Vladimir Egorov and Evgeny Egorov

Additional information is available at the end of the chapter

Abstract

Ion beam material diagnostic possibilities are discussed. Experimental data of H^+ and He^+ ion beams interaction with material for the energy range 0.8–1.6 MeV are presented. There are described the conventional ion beam analytical complex facility and some peculiarities featured for Sokol-3 IMT RAS one. Common characteristics of ion beam analytical methods are described. Specific attention is focused on the ion beam methods use for real objects investigations. It is shown that these methods are very effective for the light element diagnostics. New technology for the element surface analysis on base of the PIXE method modification by the planar X-ray waveguide-resonator application is elaborated. Attention is drowning to facts that all ion beam experimental methods are nondestructive and the Rutherford backscattering spectrometry is real quantitative analytical procedure.

Keywords: ion beam, ion beam scattering, Rutherford backscattering, RBS, ions stopping, ion acceleration, ion beam channeling, nuclear reactions, particle-induced X-ray emission, PIXE, ion beam-induced luminescence, depth elements profiles, nuclear elastic recoil spectrometry, vacuum systems, target chamber, X-ray fluorescence yield, X-ray detector

1. Introduction

It is well known that the interaction of ion beams—high energy charged particles fluxes with material is accompanied by the complex of specific effects [1]. The interaction with the solid material electron subsystem leads to uniform stopping of high energy charged particles. This interaction is not elastic owing to the atomic ionization effect initiation. Ion collisions with the atomic nuclei can have the elastic as well as inelastic character. Main channels of the interaction are presented in **Figure 1**. These channels can be used for the nondestructive quantitative analysis of studied target element composition and some features of its structure [2]. In result
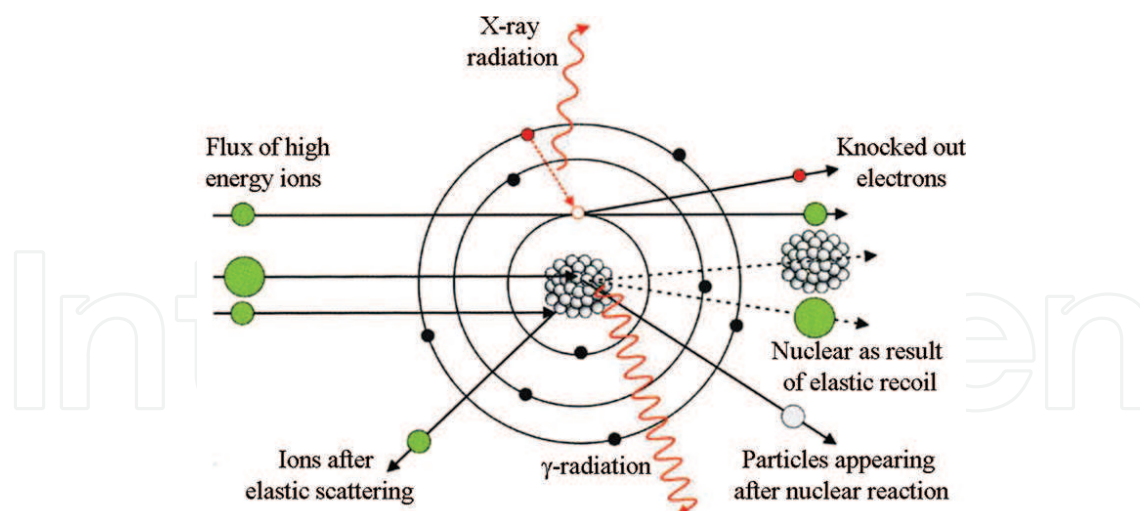
Figure 1. Products of the high energy charged particles interaction with atoms flux.

of the ion beam stopping the material, electron subsystem comes into the excited state. The excited state relaxation can happen by the radiation mechanism through luminescence. The optical luminescence spectra analysis allows to characterize some features of the studied material band structure [3–5]. More high energy relaxation leads to the X-ray characteristic fluorescence irradiation. Collection of X-ray fluorescence spectra is the subject of the particle-induced X-ray emission (PIXE) spectrometry [6–8].

The elastic interaction of high energy ion with atomic nucleus is described by the Rutherford expression, which presents fundamental basis for the Rutherford backscattering (RBS) spectrometry [8–14]. This type of ion-nucleus collision allows to create the nucleus elastic recoil spectrometry [15, 16]. The inelastic ion-nucleus collision leads to the nucleus excitation and the nuclear reaction provoking [17, 18]. Specific peculiarity of the ion-nucleus interaction is the nonRutherford scattering effect [19]. This effect is connected with the increase in time interaction and change in scattering conditions. It must be taken into account to use the proton beam scattering on nuclear of light elements at energy range 0.5–2.0 MeV. In such cases, this effect can be used for the increase in analytical efficiency for the light element diagnostics.

The above enumerated techniques based on interaction of chargedparticles beams with substance are indifferent to the material structure peculiarities. At the same time, experimental investigations showed that the monocrystalline and epitaxial targets study by ion beam analytical methods demonstrate specific deviations from results characteristic for polycrystalline and amorphous ones. The monocrystalline structure is characterized by long-range open spaces through the ionsthat can propagate without significant scattering and diminished stopping. Ions can spread to these open channels by glancing collisions with the atoms rows or planes, hereby extending the final ion distribution deeper into target. This effect was called the ion beam channeling, which can be the axial or planar one [20, 21]. The axial channeling of ion beam is visualized in**Figure 2**. The channeling effect can be used to the trace impurities diagnostics in single crystal and epitaxial targets, the structure defects analysis and for the position determination of impurity atom in the structure. Moreover, this method can allow to define the relative angular orientation of the unit cells axis within the layers of multilayer
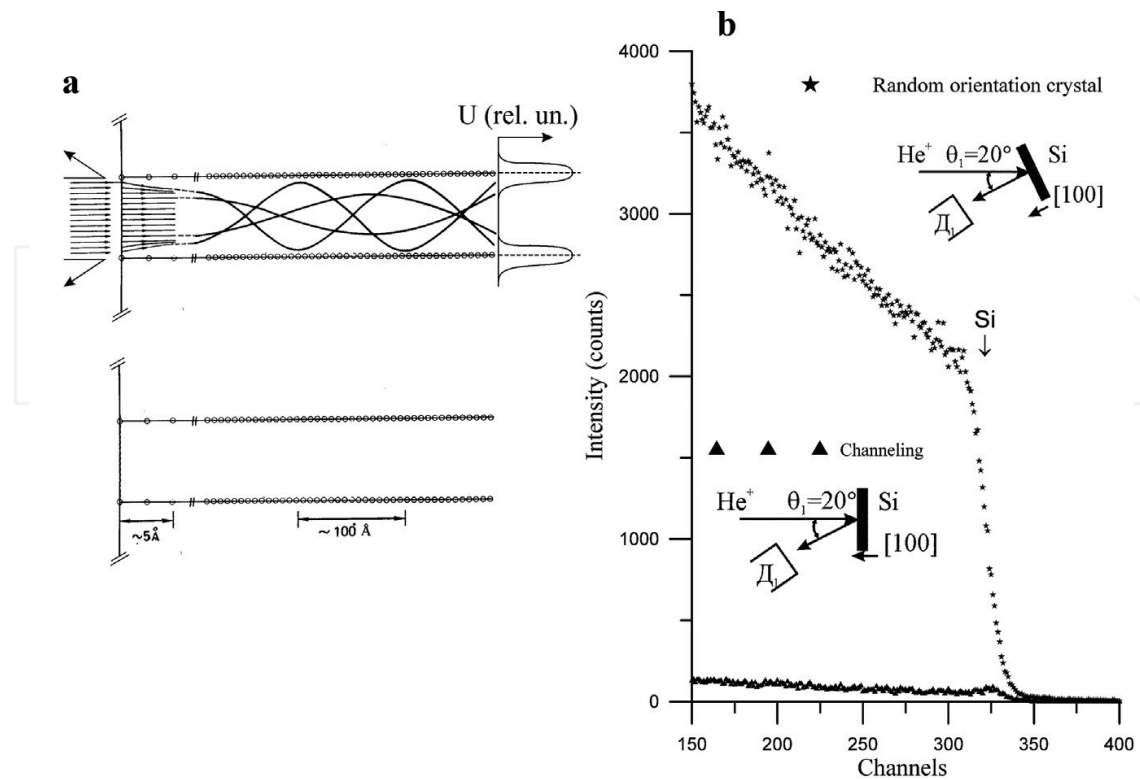
Figure 2. The model of He$^+$ ions flux axial channeling through Si monocrystal along [100] crystallographic axis (a) and RBS spectra He$^+$ ions flux for Si crystal in random position about the ion beam propagation direction and in conditions of the ion beam channeling along [100] its axis (b).

heterostructures [22]. The ion beam channeling is accompanied by the excitation processes efficiency reduction connected with inner atomic electrons of the target. X-ray fluorescence yield intensity excited by high energy beams comes down. At the same time, the intensity of ionoluminescence increases. In the ion beam channeling conditions, the nuclear reaction efficiency and probability of the nuclear recoil effect reduce to a minimum.

Ion beam experimental methods of the material diagnostics are realized by use of ion beams analytical complexes Sokol-3. This complex is in our disposal and will be shortly described in the next section.

2. Experimental setup for ion beam measurements

Common arrangement of the Sokol-3 units is presented in **Figure 3**. The Van de Graaff electrostatic generator, which can generate H$^+$ and He$^+$ ion fluxes in the energy range 0.05–2.0 MeV with energy dispersion $\Delta E = 0.1/0.3$ keV, is the most important device of the ion beam analytical complex. The generator allows to vary of the ion beam current magnitude from 0.1 to 50,000 nA (from $6 \cdot \times 10^8$ to $3 \cdot \times 10^{13}$ ions/s) in the beam spot on studied target with diameter 0.1–5 mm. The ion beam current magnitude stability is 3–5%. The analytical complex is equipped by the vacuum system with total volume near 1 m^3. The clean vacuum environment in ion guides and experimental chambers is provided by turbomolecular and magnetic-discharge pumps
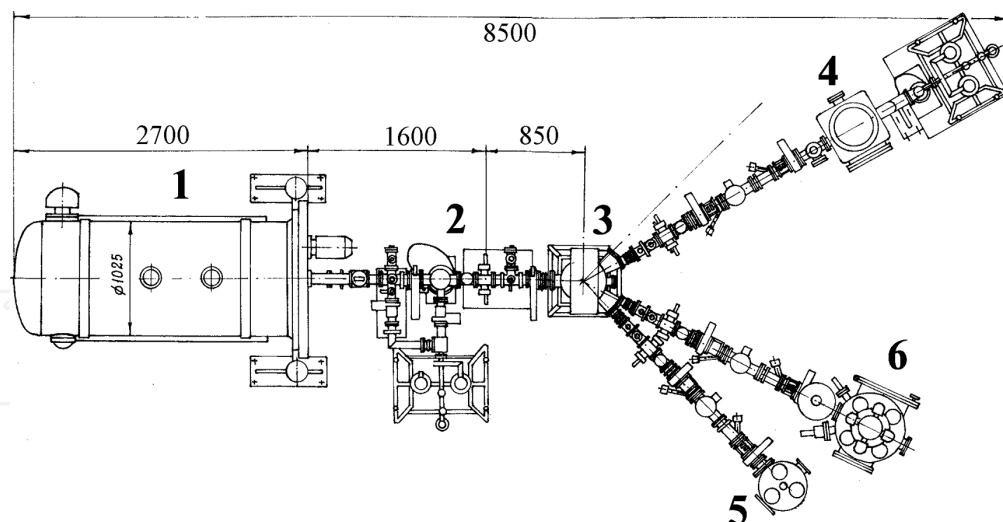
Figure 3. Units arrangement of Sokol-3 ion beam analytical complex facility. 1. Van de Graaff accelerator ESU-2; 2. Vaccum ion guide; 3.Analytical electromagnet; 4.RBS chamber; 5.Chamber for nuclear recoil spectrometry; 6.Chamber for PIXE and ionoluminiscence measurements.

working in a pair with additional use the liquid nitrogen freezing out. In the result, the medium residual pressure in the vacuum system is usually near 1×10^{-6} torr (7×10^{-4} Pa). At the same time, experimental investigations in the complex chambers are accompanied by C-H film appearing in the ion beam spot. It is connected with great number of the vacuum joints with rubber-like gaskets. Any ion beam analytical complex must be provided by the analytical magnet for the ion beams turning into experimental chambers. Our analytical complex is equipped by three experimental chambers for the RBS, nuclear reaction, and channeling measurements, for the registration of the nuclear recoil effects and for the PIXE and ionoluminescence spectrometry. The Rutherford backscattering is characterized by the original system of the studied target scattered ions registration. It has two detectors for the ions fluxes parallel registration on angles $\theta_1 = 167°$ and $\theta_2 = 125°$ to the initial direction of ion beam propagation as shown in **Figure 4**. Furthermore, the figure presents experimental and theoretical RBS spectra of He$^+$ions for Nb/Si target obtained for the angles pointed above. It is very important that two independent RBS spectra represent the target element distribution. The spectra approximation carried out by RUMPP computer program built on base of the RUMP software modification [23] allowed to obtained the target depth element concentration profile. The depth element profile of this target is very simple and the double detector registration system application in this case has an excessive character. But the approximation of two RBS spectra allowed to increase precision of the Nb thin film thickness. Application of two detector systems for RBS investigations and for registration of the nuclear reaction products allows to avoid possible errors at the experimental data interpretation.

We used the original construction for the PIXE measurements modification. **Figure 5a** presents chamber for conventional PIXE measurements execution. The conventional PIXE spectrometry allows to characterize the volume element composition of studied target. The method modification by application of the planar X-ray waveguide-resonator (PXWR) presents possibilities of the target surface element composition study [24]. **Figure 5b** shows the measurement scheme dedicated for the surface element study. PXWR can transport X-ray
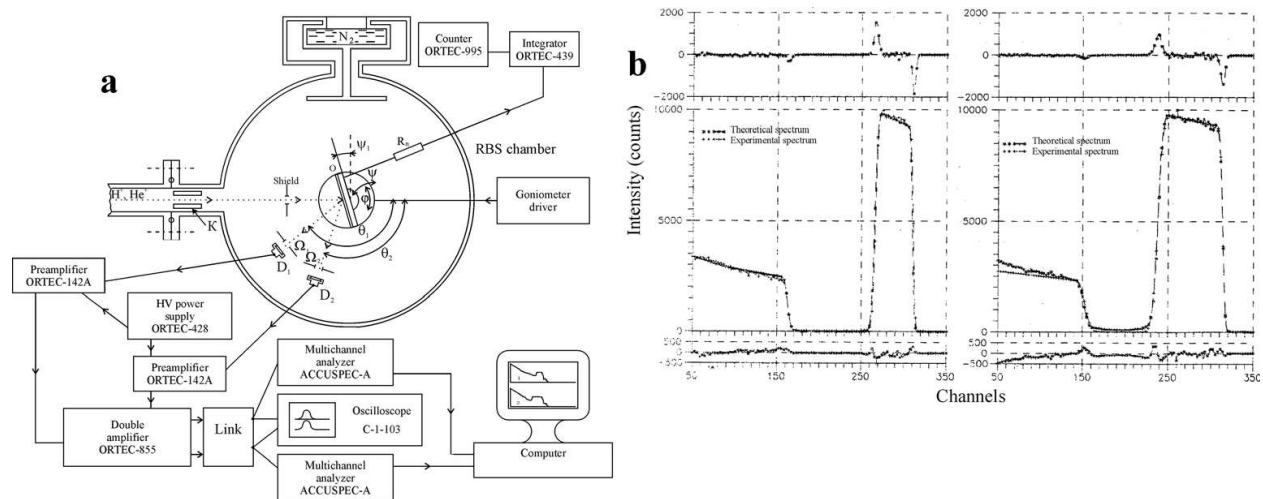
Figure 4. Schematic design of RBS chamber of Sokol-3 analytical complex equipped by two charge particle detectors (a) and pattern of application for study of Nb thin film with thickness t=135.20.7 nm on Si substrate (b).

quasimonochromatic radiation according to the waveguide-resonance mechanism of radiation flux propagation [25]. The waveguide-resonator showed in **Figure 5b** is formed by the Be polished reflector and surface of the studied target. The distance between Be reflector and target surface is equal 0.15 μm. Be reflector has the hole for the exciting ion beam propagation to the target. The extended slit clearance formed by Be reflector and target surface captures radiation from the target X-ray fluorescence yield corresponding to the surface atoms fluorescence yield and transports it into SDD X-ray detector. Similar measurement geometry for the surface elements diagnostics at ion beam excitation presents
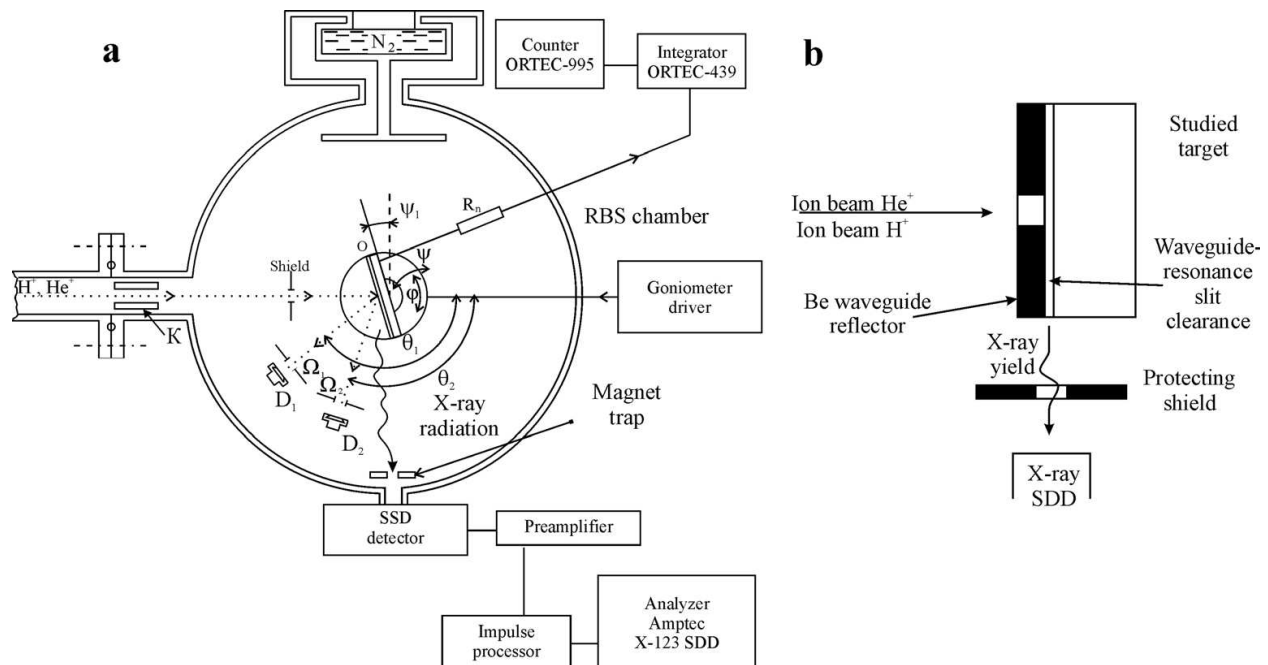

Figure 5. Experimental chamber for the PIXE conventional measurements (a) and scheme of the modifies PIXE one allowed to study of the surface element composition (b).
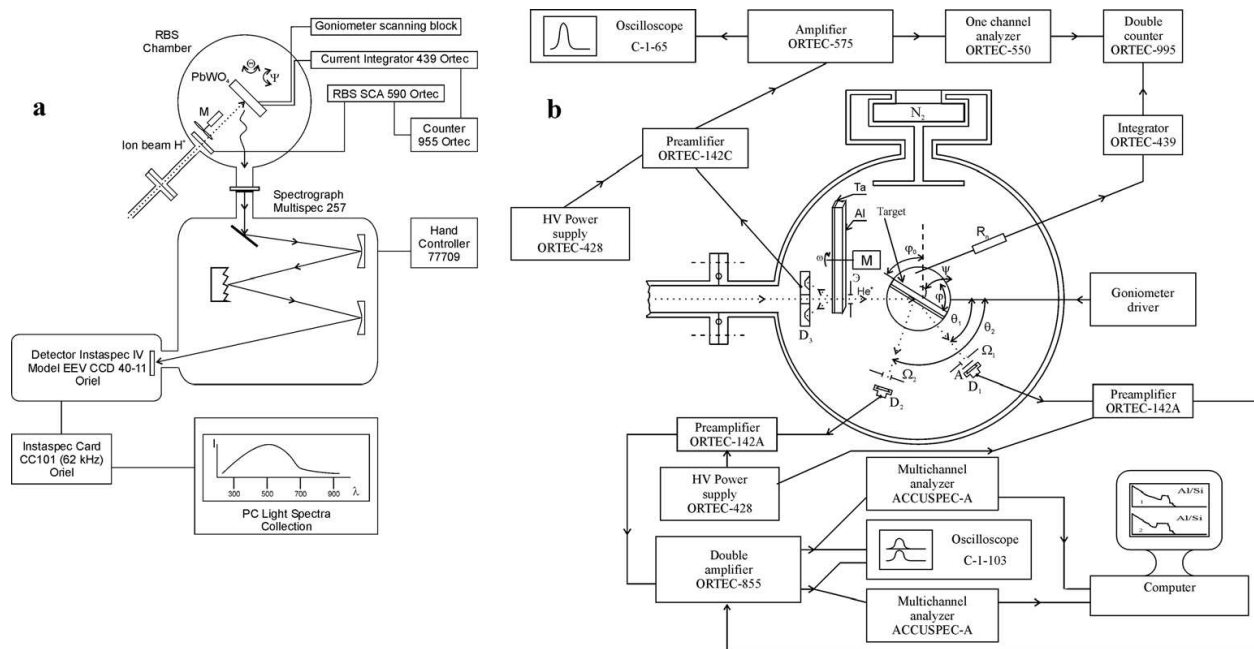
Figure 6. Schemes of experimental setups for yield registration of the light luminescence from the studied target at ion beam excitation (a) and for the target parallel investigation by RBS and the elastic nuclear recoil methods (b).

new experimental method, which was named as the total X-ray reflection fluorescence at particle excitation (TXRF PE).

Figure 6 shows the experimental chamber arrangement for the ionoluminescence and the nuclear recoil spectrometry. These investigation methods are realized in frame of the Sokol-3 facility in conventional arrangement.

Experimental investigations of the ion beam channeling can be executed in any chambers of the analytical complex. But most part of these experiments is carried out by using the RBS chamber.

3. Rutherford backscattering spectrometry as the basic method of material ion beam diagnostics

3.1. Common principles of the method

The Rutherford backscattering conception is based on possibility of the energy losses direct calculation for ion beams interacting with electron and atomic nuclear material subsystems. The energy redistribution in the ion-nucleus collision is defined by the kinematical factor expression [10]:

$$E_1 = E_0 \left[\frac{\sqrt{M_2^2 - M_1^2 \sin^2\theta} + M_1\cos\theta}{M_1 + M_2} \right] \tag{1}$$

where E_0 and E_1 are energies of ion pre- and post-collision, M_1 and M_2 are masses of ion and nucleus accordingly and θ is the angle of ion deviation from its initial propagation direction.

There is discussed the "backscattering" situation because the kinematical factor maximum magnitude is obtained for θ near 180°. In this case, we have the best mass resolution.

Probability of the ion-nucleus collision is defined by the Rutherford famous formula in form of the scattering average differential cross-section σ, which can be presented in the laboratory coordinates system by the next expression [8]:

$$\sigma = \frac{Z_1 Z_2 e^2}{2E} \frac{\sqrt{1 - x^2 \sin^2\theta} + \cos\theta}{\sin^4\theta \sqrt{1 - x^2 \sin^2\theta}} \tag{2}$$

where x is M_1/M_2 relation, Z_1 and Z_2 are changes of ion and nucleus, e is the electron charge and E is the ion pre-collision energy. The charge particle detector registers the total particles quantity A_i, which defines by the collision cross-section, the total quantity of charged particles interacted with the studied target q, the detector spatial angle Ω, the volume atomic concentration N_i and the layer thickness t connected with the RBS spectrum discreteness degree and can be presented by the expression [8]:

$$A_i = q\Omega\sigma N_i t \tag{3}$$

Total Rutherford backscattering spectrum presents aggregate of similar magnitudes outlined in the diagrammatic form. Sample of this similar diagram is shown in **Figure 7**. RBS spectra of He^+ and H^+ ion beams obtained for the $SrTiO_3$ stoichiometric target are presented. These spectra are diagrams reflecting dependences of the ion beams scattering yield on the energy of scattering particles. Every channel of the diagrams reflects the ions number scattering on nuclei the target atoms (Eq. (3)). An energy scales of the spectra are connected with the depth
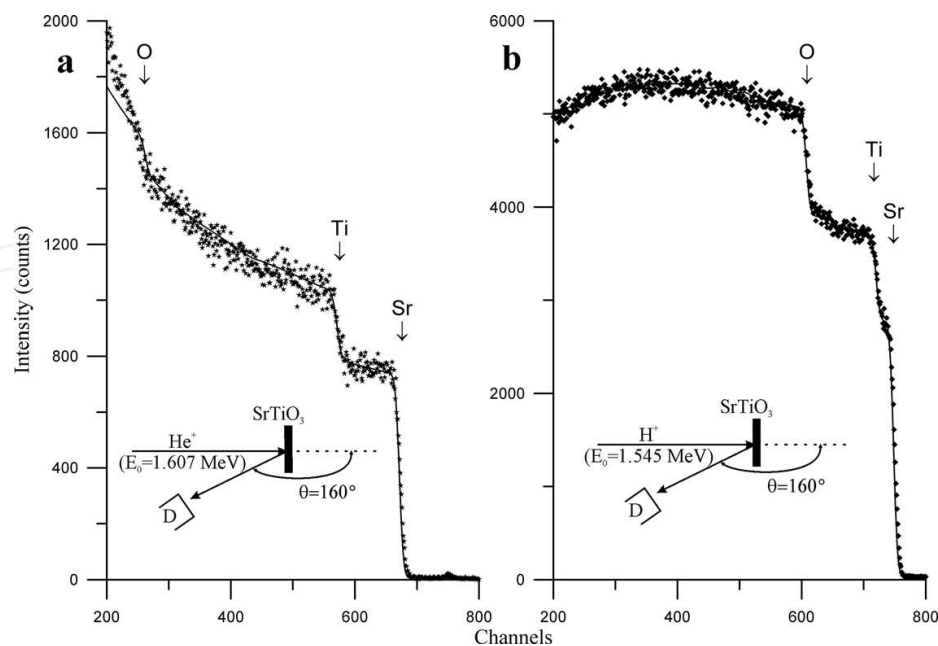

Figure 7. RBS spectra of He^+ (a) and H^+(b)ion beams obtained for the $SrTiO_3$ stoichiometric target. Experimental spectra are approximated by RUMPP program and the theoretical spectra are superposed with experimental ones. The arrows designate the scattering energies corresponding to atoms on the target surface. The measurement geometry is shown on the inserts. The energy step is 1.9 keV/channel.

elements distribution profile for the studied target. The scattering energy for surface atoms is defined by the kinematical factor, only. These energies are connected to steps edges of the diagrams. The scattering description of ion beams on nuclei of the internal atoms demands taking into account the ions stopping as pre- and post-scattering act. The stopping energy losses ΔE on the distance Δx are usually described by the Bohr formula:

$$-\frac{\Delta E}{\Delta x} = \frac{4\pi Z_1^2 e^4 n}{mv^2} \ln \frac{2mv^2}{I} \tag{4}$$

where Z_1 and v are the charge and velocity of the stopping ion, e and m are the charge and mass of electron and n is the studied material electron density. I is the ion average energy loss for the electron excitation (near 30 eV). I and n parameters are not constants and depend from very much factors. As a result, the decision was made to present the stopping losses in the tabular form [26]. This approach allowed to calculate the energy losses by introduction of the $[\bar{\varepsilon}]$ effective stopping cross-section accordingly to the expression [27].

$$\Delta E = [\bar{\varepsilon}]Nt \tag{5}$$

where N is the atomic density (atoms/cm^3). In case of the multielement material, the stopping cross-section is defined accordingly to the Bragg rule:

$$\varepsilon^{AmBn} = m\varepsilon^A + n\varepsilon^B \tag{6}$$

Accuracy of tabular magnitudes for the material stopping cross-section is limited by value near 1%. In the result, the material parameters determination accuracy cannot be better of this value. In the practical work, the stopping cross-section data are fed into a computer program providing the RBS spectra approximation [23, 27]. As a result, we have that every channel of the spectrum is connected with a planar layer of the target with thickness t and average element concentration N. The rise steepness of steps in the RBS spectrum is defined by the detector energy resolution used for the spectrum registration. The resolution of He$^+$ ions scattering fluxes is near 10 keV thatcorresponds to the depth resolution 10–12 nm at the ion beam vertical incidence on the studied target and up to 2 nm at the sliding incidence.

The Rutherford backscattering spectrometry is very effective method of the thin film structure analysis. **Figure 8** demonstrates experimental and theoretical spectra of RBS He$^+$ ion beam for SrTiO$_3$ thin film on the silicon substrate with oxidizing layer. The experimental spectrum theoretical approximation showed that the film is characterized by the stoichiometric composition with thickness t = 230 nm. Theoretical approximation of the spectrum did not involve some difficulties, because the film material contained elements with high atomic masses, and substrate, on the contrary, contained light elements. Similar situation can be observed in **Figure 9**. It demonstrates experimental and theoretical RBS of He$^+$ and H$^+$ ion beams spectra for the Hf/Cr/Al multilayer target. Theoretical approximation of these spectra showed that the Hf film had thickness t = 120 ± 5 nm and contained 11% of Sr atoms and 14% of Ti atoms. Cr film had not admixture. It was characterized by the thickness t = 40 ± 7 nm. Interdiffusion zone between these films had the thickness near 25 nm. The surface roughness of the coating was
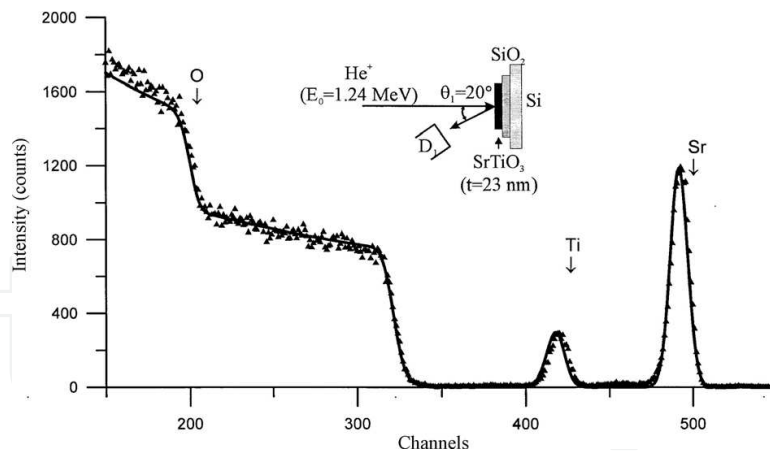
Figure 8. Experimental and theoretical RBS He$^+$ ions (E$_0$ = 1.24 MeV) spectra for the SrTiO$_3$/SiO$_2$/Si thin film structure. Arrows show the ion scattering energies on nuclei of atoms located on the target surface. Measurement geometry is shown on insert. Energy step 1.9 keV/channel.
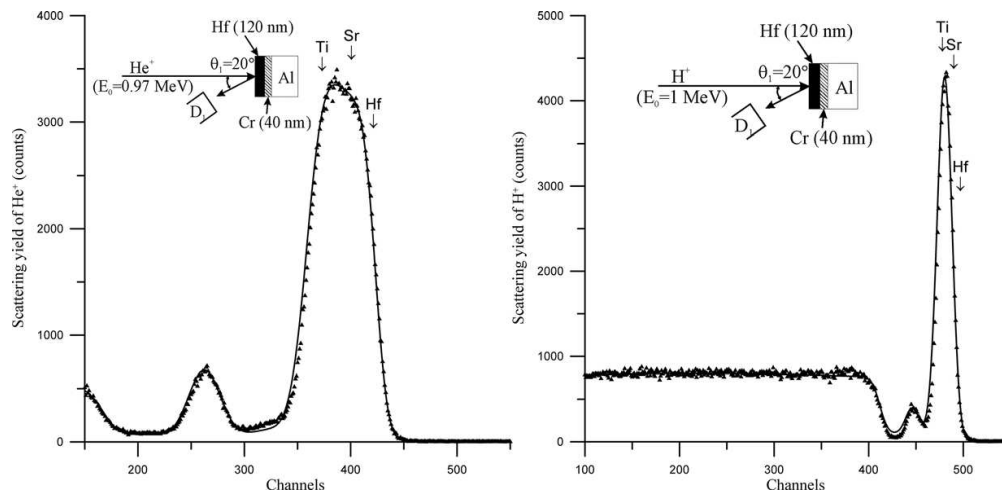

Figure 9. Experimental and theoretical RBS He$^+$ and H$^+$ ions spectra for the Hf/Cr/Al multilayer target. Arrows show the ion scattering energy on nuclei of atoms located on the target surface. Measurement geometry is shown on inserts. Energy step 1.9 keV/channel.

near 20 nm. Last parameter was evaluated on base of the steepness evaluation of step increasing for Hf(Sr, Ti) partial spectrum in comparison with this parameter for the Nb/Si standard target with roughness smaller 5 nm. The surface roughness Δr can be evaluated by the next expression [10]:

$$\Delta r = \frac{\sqrt{\Delta E_{\exp}^2 - \Delta E_d^2}}{N_t[\bar{\varepsilon}]} \tag{7}$$

where $\Delta E_{\exp}$ is the half width of the curve obtained as a result of the step rise steepness differentiation, ΔE_d is the detector energy resolution, N_t is the target atomic density and $[\bar{\varepsilon}]$ is the average value of the target atomic cross-section. Comparison of the RBS spectra obtained

for the same object shows that the He$^+$ ion beam application allows to have the better resolution and the H$^+$ ion beam use takes possibilities to test object on the more depth.

3.2. Possibilities of the RBS elements diagnostics

The RBS investigations of target with the heavy elements high content have evident problems. **Figure 10** presents RBS H$^+$ and He$^+$ ions beam spectra for the $W_{0.45}C_{0.43}C_{0.12}$ target characterized by the tungsten atoms high concentration. The scattering cross-section of ions on the W nuclei is higher in comparison with these parameters for C and Co atomic nuclei. The alloy target composition had been gained in the result of the four spectra joint approximation obtained for He$^+$ and H$^+$ ion scattering beams collected for $\theta_1 = 167°$ and $\theta_2 = 125°$. The nonRutherford scattering effect was taken into account in the calculation. Owing to the necessity of this effect inclusion, specific investigation were executed [18, 19]. Sample of similar investigations of $^{12}C^6$ nucleus nonRutherford scattering factor is presented in **Figure 11**. Comparison of the Rutherford scattering cross-section and magnitudes of this parameter obtained in the experiments shows a great difference especially for the energy E = 1735 keV. The nonRutherford scattering factor value depends on the registration angle, and it is a need to get the factor experimental data for the selected measurement conditions. Similar work of the nonRutherford factor determination for carbon and boron atoms was executed preparatory to approximate RBS spectrum presented in **Figure 12**. The approximation of this spectrum is not simple procedure. Chief problem of the approximation is connected with the nonRutherford factors energy variation for carbon and boron atoms. The approximation result is presented in the table. Total thickness of the coating is 1.75 μm. Including the second RBS spectrum into approximation procedure does not improve the final result because this procedure demands additional investigations for receiving the nonRutherford factors energy dependences for the additional scattering angle. At the same time, the nonRutherford factor can be very useful for the
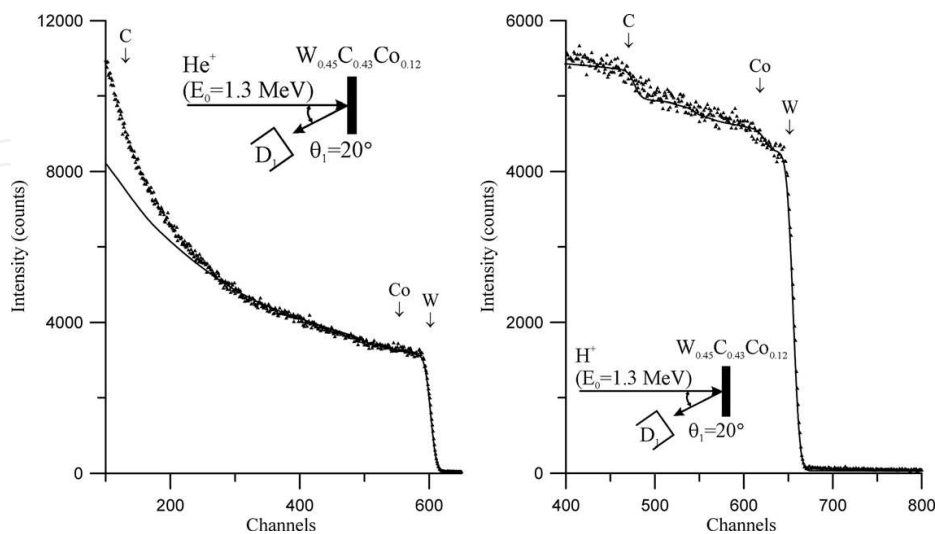

Figure 10. Experimental and theoretical RBS He$^+$ and H$^+$ ions spectra for the $W_{0.45}C_{0.43}Co_{0.12}$ high temperature alloy. Arrows show the ion scattering energies on nuclei of atoms located on the target surface. Measurement geometry is shown on inserts. Energy step 1.9 keV/channel.
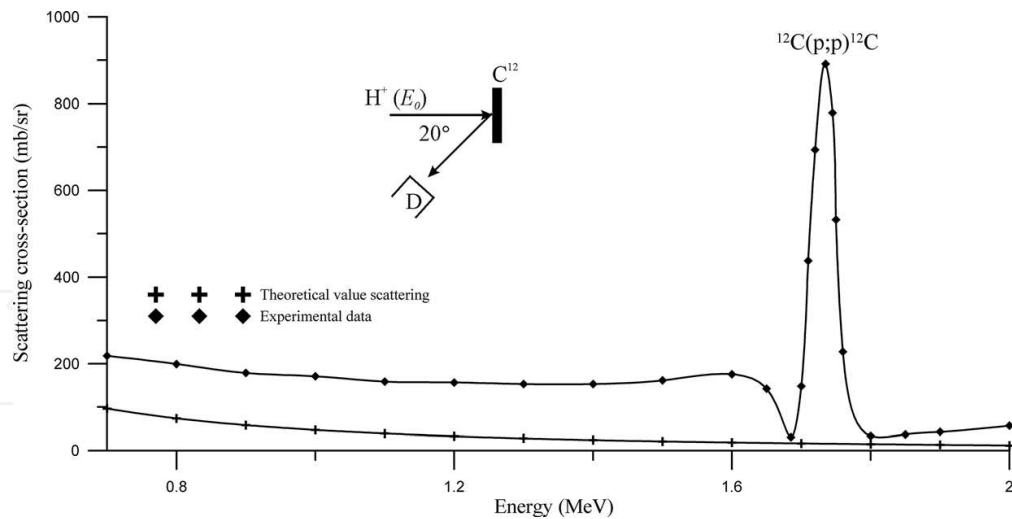
Figure 11. Theoretical and experimental energy dependences of H^+ ion beam scattering cross-section on ^{12}C nuclei for the collection angle $\theta = 167°$.
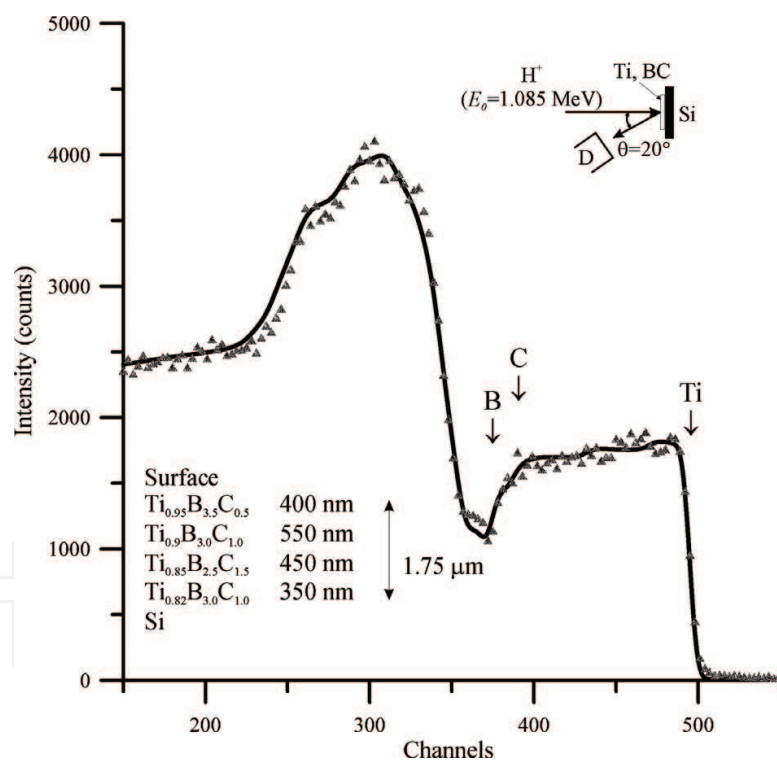

Figure 12. Experimental and theoretical RBS H^+ ions ($E_0 = 1.085$ MeV) spectra for Ti-B-C film deposited on Si substrate in result of the Ti_2CB_{10} sample magnetron sputtering (a) and table with the approximation results. Arrows show the ion scattering energies on nuclei of atoms located on the target surface. Measurement geometry is shown on insert. Energy step 1.9 keV/channel.

targets study containing light element. As the sample, RBS spectra of the polished beryllium disk are presented in **Figure 13**. The spectrum of the He^+ ions scattering in selected energy range does not distort by the nonRutherford factor. It shows that the target possesses the surface oxide film
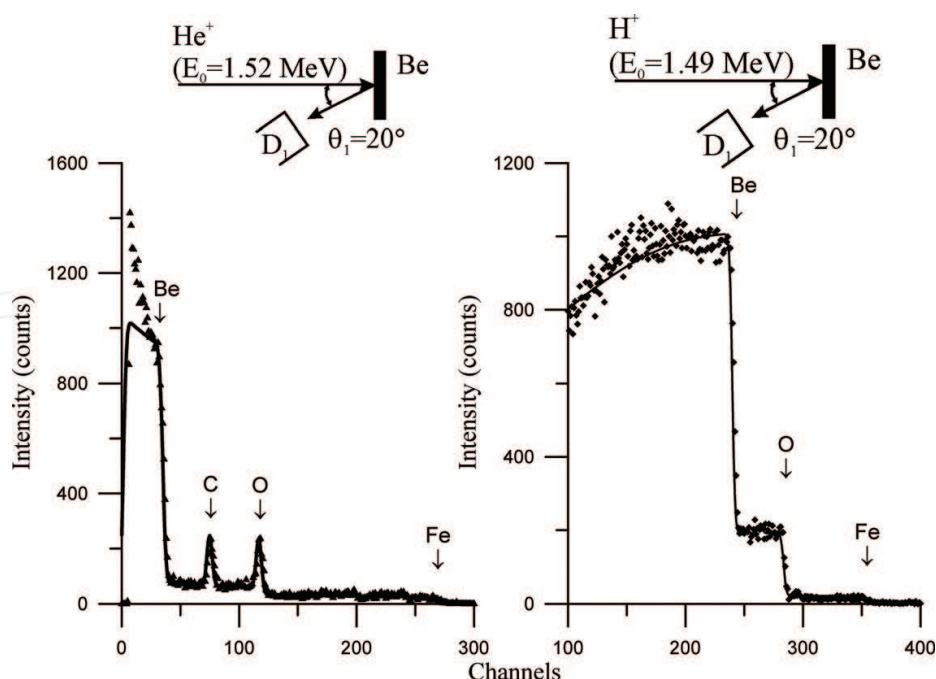
Figure 13. Experimental and theoretical RBS He$^+$ and H$^+$ ions for the polished Be disk. Arrows show the ion scattering energies on nuclei of atoms located on the target surface. Measurement geometry is shown on inserts. Energy step 3.8 keV/channel.

with thickness near 10 nm and the carbon hydrogen snuff with similar thickness appearing in result of the ion bombardment. The beryllium material contains 5% of the oxygen atoms, 0.1% of the iron atoms and 0.002% of the tungsten atoms. RBS spectrum of H$^+$ ions confirms these results. But its approximation is more difficult and it does not show the oxide film on the disk surface. At the same time, its registration time is more short in comparison with the He$^+$ spectrum collection.

Be polished disks can serve beautiful substrates for study of the solution dry residues and structures prepared by the specific procedure. Sample of the similar investigation is presented in **Figure 14**. This target is studied by RBS method and by application of the elastic nuclear recoil spectrometry. The main element composition of the petroleum film is $H_{0.07}C_{0.90}S_{0.028}N_{0.002}$. The film admixture composition defined by PIXE method will be discussed below. RBS spectrometry can be used for the medical preparation element diagnostics. **Figure 15** shows experimental and theoretical of RBS spectra for the solution dry residue of pantocrine in form of the film on Be substrate. The element composition knowledge is not chief problem for the pharmacology, but RBS, PIXE and nuclear reaction analysis can help for the specific element diagnostics of medical preparations.

Figure 16 shows experimental and theoretical RBS spectra for the graphene oxide film deposited on the Be substrate in the hydrothermal conditions. The technology of the grapheme oxide preparation is not perfect. As a result, the film contains Na and Ca atoms in the macro concentration. At the same time, RBS measurements allow to control the admixtures macro concentration presence and the film constitution. RBS method is useful for the target study containing other light element. **Figure 17** presents experimental and theoretical RBS He$^+$ and H$^+$ ions spectra for the hexagonal BN target. Mathematical approximation of the spectra shows
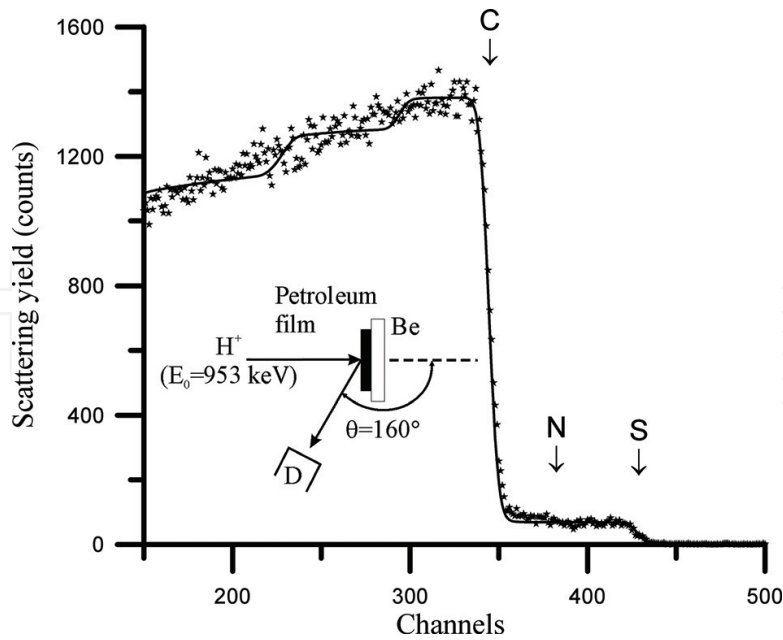
Figure 14. Experimental and theoretical RBS H$^+$ ions (E$_0$= 0.953 MeV) spectra characterizing the petroleum film on Be substrate. Film composition is H$_{0.07}$C$_{0.9}$S$_{0.028}$N$_{0.002}$ (on mains elements). Arrows show the ion scattering energies on nuclei of atoms located on the film surface. Measurement geometry is shown on insert. Energy step 1.9 keV/channel.
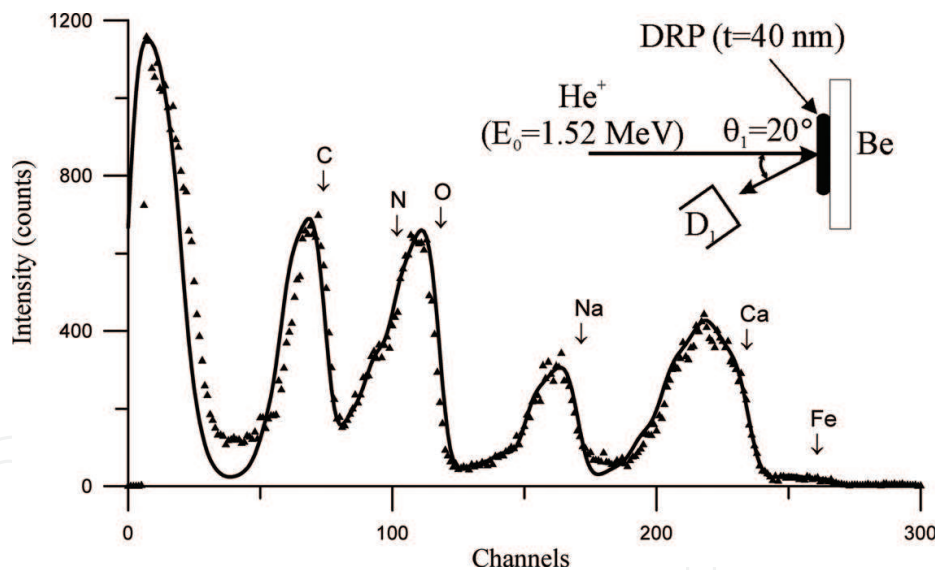

Figure 15. Experimental and theoretical RBS He$^+$ (E$_0$ = 1.52 MeV) ions spectra for the dry residue of pantocrine (DRP) aqueous solution on Be substrate. Arrows show the ion scattering energies on nuclei of atoms located on the dry residue film surface. Measurement geometrics and the pantocrine element compositions are presented on inserts. Energy step 3.8 keV/channel.

that the surface layer of the target has the boron increasing concentration. The spectrum of H$^+$ ions scattering showed that the scattering process is accompanied by the ^{11}B(p,α)^{8}Be nuclear reaction course. The approximation has some problem in the context of ^{10}B^5 and ^{11}B^5 boron two isotopes existence in comparison concentrations. Every isotope is characterized by its own
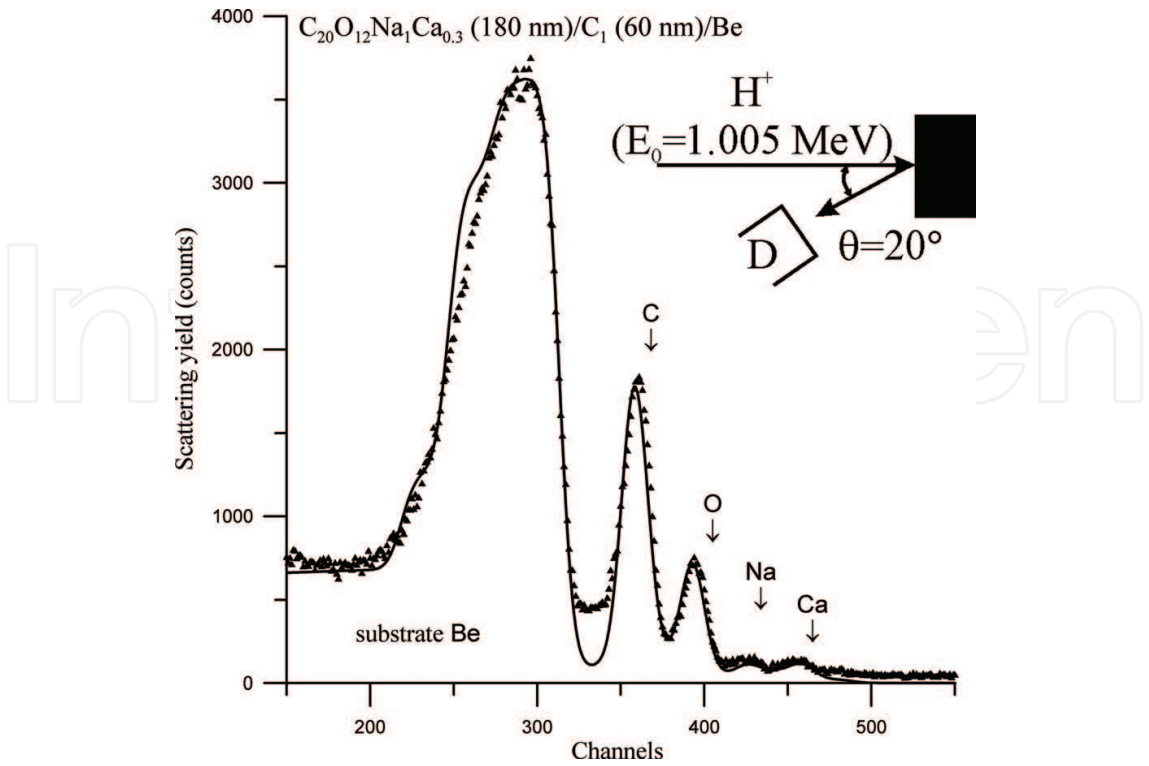
Figure 16. Experimental and theoretical RBS H$^+$ (E$_0$ = 1.005 MeV) spectra for the graphene oxide film deposited on the beryllium substrate in hydrothermal conditions. Arrows show the ion scattering energies on nuclei of atoms located on the film surface. Measurement geometries and the film parameters are presented on insert. Energy step 1.9 keV/channel.
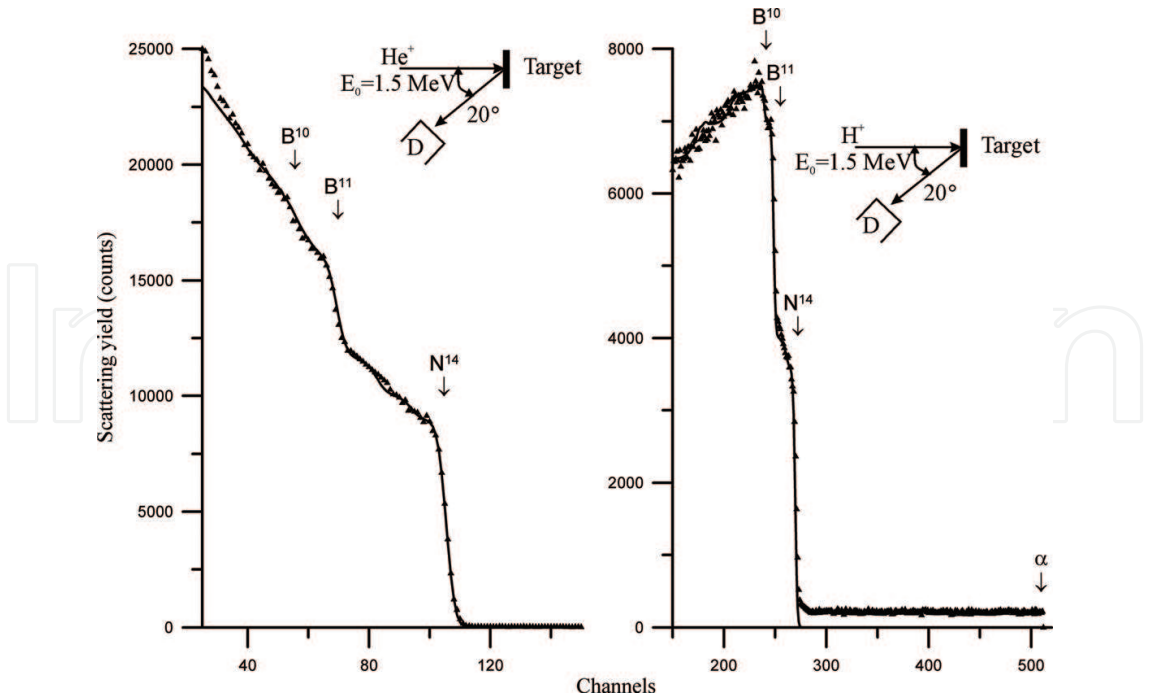

Figure 17. Experimental and theoretical RBS He$^+$ and H$^+$ ions (E$_0$ = 1.5 MeV) spectra for the Boron-Nitrogen target prepared by chemical exfoliation method in form of the free plate. Arrows show the ion scattering energies on nuclei of atoms located on the plate surface. Measurement geometry is shown on insert. Energy step 3.8 keV/channel.
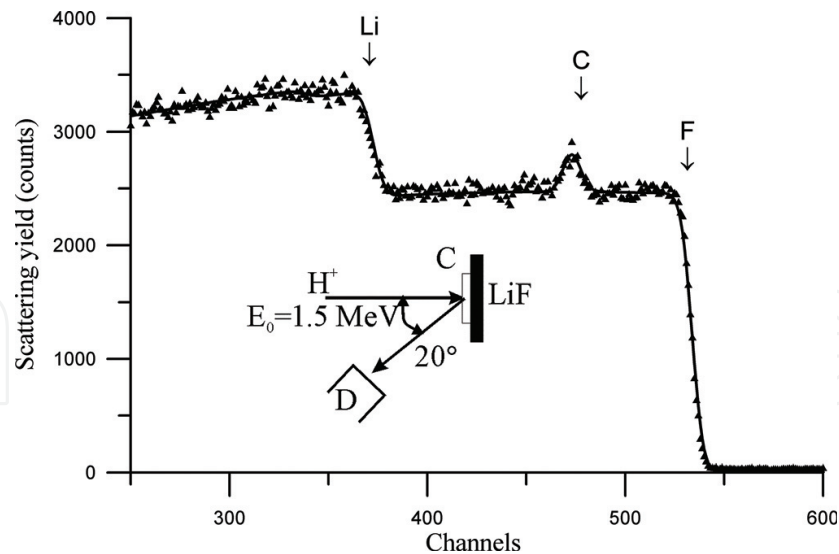
Figure 18. Experimental and theoretical RBS H⁺ions spectra for the LiF natural specimen. Surface carbon film with thickness t = 12 nm appeared during of the measurements process. Arrows show the ion scattering energies on nuclei of atoms located on the target surface. Measurement geometry is shown on insert. Energy step 1.9 keV/channel.

nonRutherford factors for the proton beam scattering. The nuclear reaction existence can be used for the boron concentration diagnostics in materials.

The Rutherford spectrometry can help to analyze the lithium atoms presence in materials. **Figure 18** shows RBS spectrum for the LiF stoichiometric target. This approximation required the nonRutherford data collection in the selected energy range for the H⁺ ion beam scattering on Li and F atomic nuclei. But owing to the nonRutherford factor for Li, N, O and F atomic nuclei is not great the diagnostic of its atoms in targets with high concentration of heavy atoms presents some difficulties (see **Figure 10**). PIXE and ion beam channeling methods can help in this problem solution.

3.3. Atomic diffusion study by RBS method

Study of atomic diffusion peculiarities in solid material is the main branch of the solid state physics [28]. The wide use of thin material films has direct relation to study the material transport in thin films and coatings, since the density of short-circuit diffusion paths, especially grain boundaries (GBs) in its compositions is higher as compared with massive materials [29]. In our work, we used RBS spectrometry possibilities for the interdiffusion study in the Au/Cu bimetallic structure. **Figure 19** presents RBS He⁺ spectra of the bimetallic structure pre and post treatment used different thermal actions [30]. At the long thermo treatment, the main interdiffusion mechanism was connected with the bulk diffusion (**Figure 19a**). In this case, the Au/Cu interface disappears and the intermediate layer arises. In case of the short high temperature treatment, we can see the copper atoms on the target surface, and Au atom from the initial interface dissolves in the Cu film. As a result, it is possible to obtain bulk and GB diffusion factors for different bimetallic combinations and to evaluate magnitudes of the possible segregation effect [31]. Particular significance for the diffusion practice can have the element isotopic investigation with the nuclear reaction application.
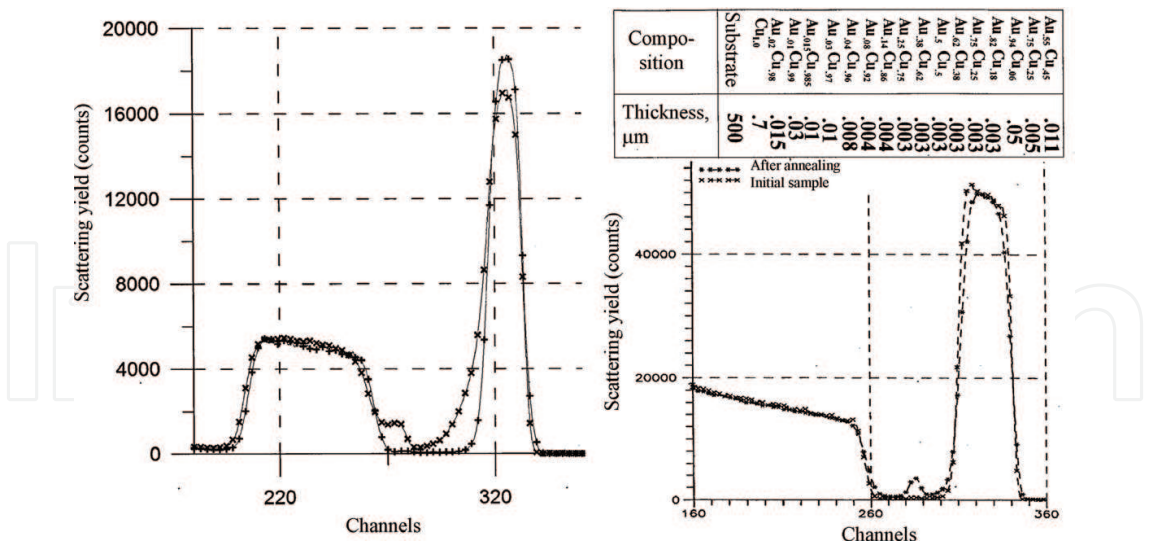
| Compo-sition | Substrate | Cu$_{1.0}$ | Au$_{.02}$Cu$_{.98}$ | Au$_{.03}$Cu$_{.85}$ | Au$_{.01}$Cu$_{.99}$ | Au$_{.01}$Cu$_{.97}$ | Au$_{.08}$Cu$_{.92}$ | Au$_{.04}$Cu$_{.96}$ | Au$_{.06}$Cu$_{.94}$ | Au$_{.08}$Cu$_{.86}$ | Au$_{.14}$Cu$_{.86}$ | Au$_{.25}$Cu$_{.75}$ | Au$_{.38}$Cu$_{.5}$ | Au$_{.42}$ Cu$_{.42}$ | Au$_{.75}$ Cu$_{.25}$ | Au$_{.8}$ Cu$_{.18}$ | Au$_{.94}$ Cu$_{.06}$ | Au$_{.75}$ Cu$_{.25}$ | Au$_{.95}$ Cu$_{.05}$ | Au$_{.45}$ Cu$_{.45}$ |
| Thickness, μm | 500 | .7 | .015 | .03 | .01 | .01 | .008 | .004 | .004 | .003 | .003 | .003 | .003 | .003 | .003 | .05 | .05 | .005 | .011 |

.... After annealing
×××× Initial sample

Figure 19. Experimental and theoretical RBS He$^+$ions spectra for the Au/Cu bimetallic structure pre and post-treatment of the thermal action. The long time treatment at T = 493 K during 2400 sec of Au (44 nm)/Cu (190 nm) led to bulk interatomic diffusion (a). The short time treatment at T = 523 K during 300 sec showed the grain boundary diffusion, only. Second case is illustrated the table of the depth element distribution. Energy step 3.8 keV/channel.

3.4. Special features of the material density analysis

The material atomic density is a principle parameter of the substance condenses state. This parameter magnitude is usually defined by direct measurement of the subject mass and volume. But this method is not suitable for the material density determination of thin film structures. The Rutherford backscattering method can help to solve this problem. The atomic density distinction must lead to variation of the RBS yield intensity. **Figure 20** shows that the
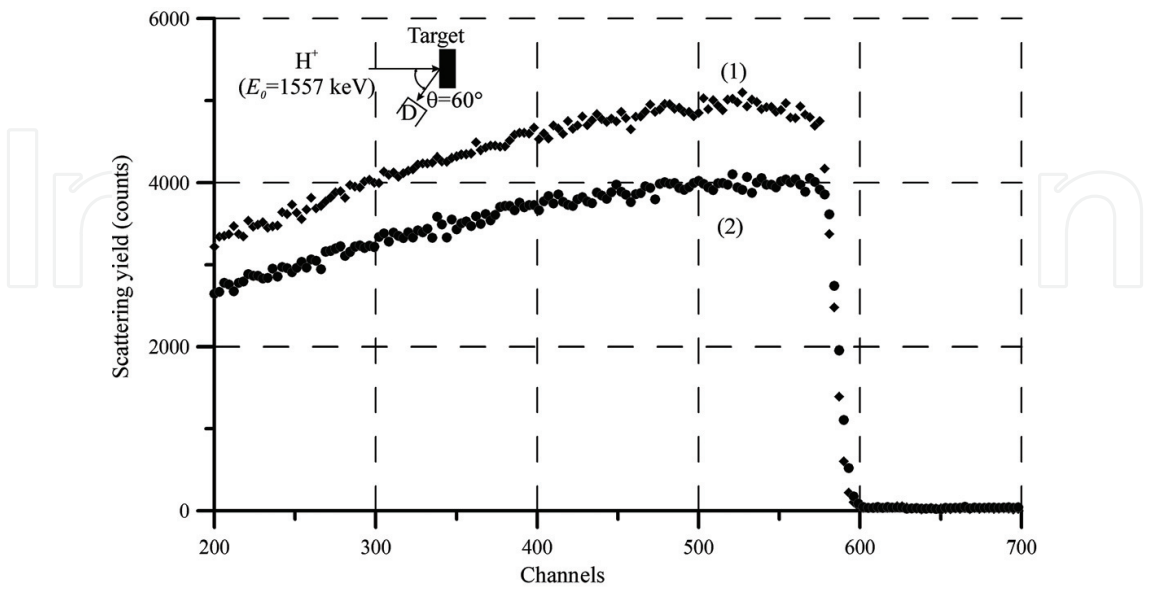
Figure 20. Experimental RBS H$^+$ ions (E$_0$ = 1.557 MeV) spectra for diamond (ρ = 3.52 g/cm^3) and glassy carbon (ρ = 2.21 g/cm^3) sample. Measurement geometry is shown on insert. Energy step 1.9 keV/channel.

expected effect takes place, really. RBS H$^+$ ions spectra for the diamond crystal and for the glass carbon sample are not equivalent. The diamond structure is characterized by a more compact atomic packing and demonstrated the enhanced scattering yield in the RBS spectrum. Its effect can be used for study of the porous structures. **Figure 21** shows the sample of the Rutherford backscattering study of the Al film in conditions after its preparation and in the result of thermal treatment [32]. Initial spectrum demonstrates the smaller scattering intensity yield in comparison with the theoretical spectrum (a). It is connected with the structure vacancy concentration near 6%. The thermal treatment let to the Al film, thickness decreasing from 300 to 284 nm (see the diagram (c)). The comparison of initial and finishing experimental spectra demonstrates the thickness decreasing and the atomic density increasing up to the normal structure value. Similar investigations is very important because the thin film preparation is no the equilibrium thermodynamic process.

The material atomic density variation can be connected with not only the structural vacancy appearing. Material in the nanostructure state is characterized by the increase in interatomic distance [33]. **Figure 22** demonstrates the Rutherford backscattering yield decreasing for the Ag thin films deposited on the silicon substrate. There are presented two RBS He$^+$ (E$_0$ = 1.27 MeV) ions spectra collected by our double detector system (θ_1 = 160°, θ_2 = 120°). Theoretical approximation of these spectra showed that the Ag film thickness is equal 48 nm but the evident discrepancy between Ag theoretical and experimental partial spectra was discovered. In this case, it was nearly equal to 6%. Moreover, the discrepancy increases as the Ag film became more slender and disappears when it will be large 100 nm. Our diffraction measurements confirmed supposition about the atomic density decreasing as aresult of the interatomic distance growth. Similar RBS investigations can be very useful for the material atomic density evaluation in multilayer structures.
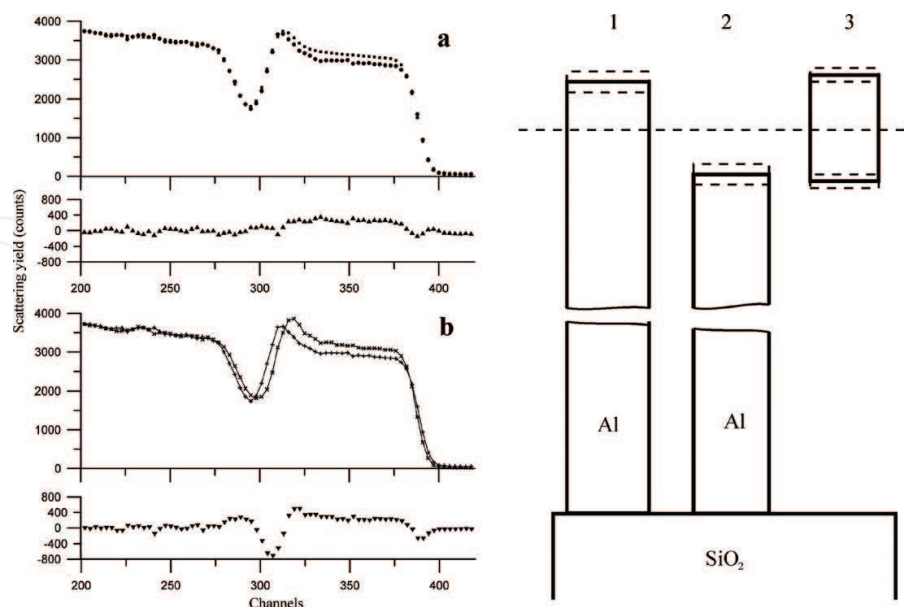

Figure 21. Experimental and theoretical RBS He$^+$ (E$_0$ = 1.5 MeV) ions for Al/SiO$_2$ structure pre (a) and post-thermal treatment (b) and the experimental diagram of the Al thin film thickness variation in result of the thermal treatment influence. Scattering angle is 160°. Energy step 1.9 keV/channel.
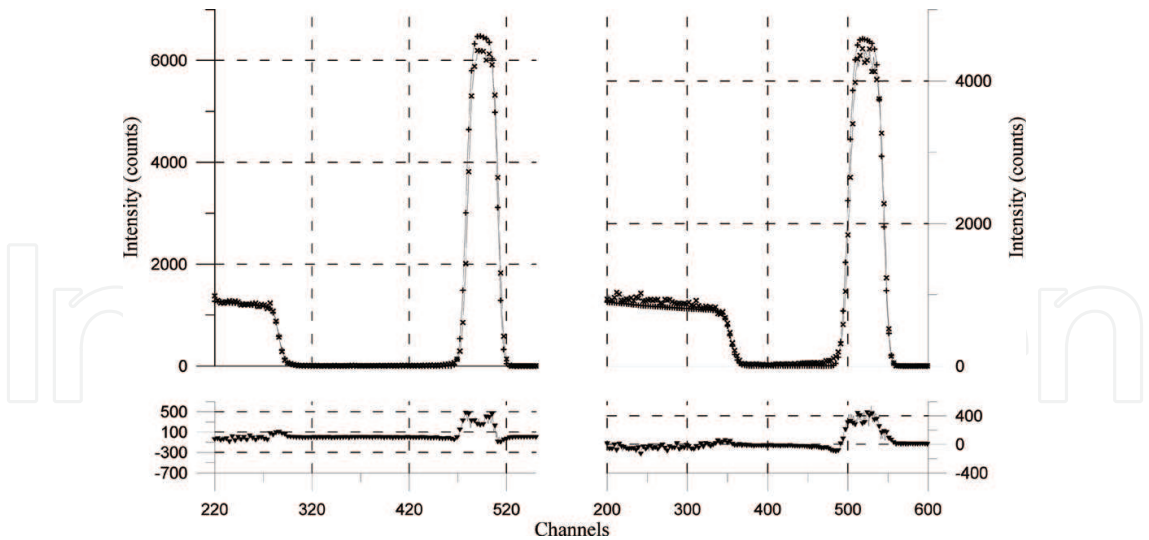
Figure 22. Experimental, theoretical and subtraction RBS He$^+$ (E$_0$ = 1.27 MeV) ions spectra for the Ag thin film deposited on Si substrate. Spectra were collected by the double detector system (θ_1 =160° and θ_2 = 120°). Measurement geometries is presented on inserts. Energy step 1.9 keV/channel.

4. Particle-induced X-ray emission

4.1. Common principles of the method

Particle-induced X-ray emission is an ion analytical method, which utilizes the X-ray characteristic yield induced by ion beam interacting with the electron subsystem of target atoms. X-ray characteristic energy depends on Z atomic number of the target atom. PIXE method similar to other X-ray fluorescence diagnostic technologies collects the characteristic lines yield corresponding to K, L and M radiation series. At the same time, the main distinguishing of the
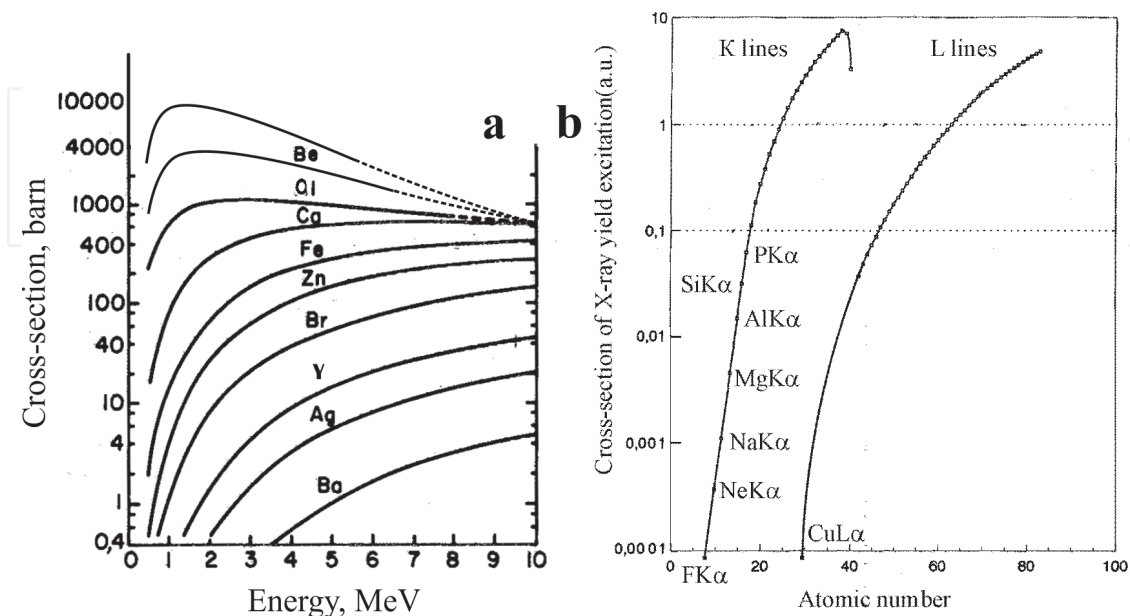

Figure 23. Cross-section of the X-ray fluorescence excitation by proton beam [34] (a) and MoKα radiation flux (b).

ion beam excitation method from X-ray, electron beams and gamma radiation ones is the very high efficiency of the low energy characteristic radiation excitation. In this plane, it is very interesting to compare the X-ray fluorescence yield excitation cross-section at use the X-ray high energy flux (MoKα, E = 17.4 keV) and the proton high energy beam. These data arepresented in **Figure 23** [34]. Cross-sections of X-ray low energy lines excitation by the MoKα radiation flux use are characterized by very small magnitudes. At the same time, these parameters in conditions of the proton beam use demonstrate high values, especially for the low energy lines excitation. Comparison of YKα and AlKα fluorescence excitation cross-section in case of the MoKα radiation flux application shows that the yttrium fluorescence excitation efficiency is higher as the aluminum one on three orders. Similar comparison of these elements fluorescence excitation cross-sections at the proton beam excitation with energy E_0 = 1 MeV shows that the situation will be changed on the reverse one. So, it is evident that the light element diagnostic difficulties at the X-ray beam fluorescence application can be compensate by use the PIXE method [35, 36]. The X-ray fluorescence excitation by ion beams is more effective not only in comparison with the X-ray hard radiation flux application. PIXE bears some similarity to the fluorescence yield electron beam excitation but it characterizes by smaller values of the bremsstrahlung photon intensity yield. As a result, PIXE measurements are distinguished by the background lower level in comparison with the electron excitation. This fact is illustrated in **Figure 24** [7]. The spectra
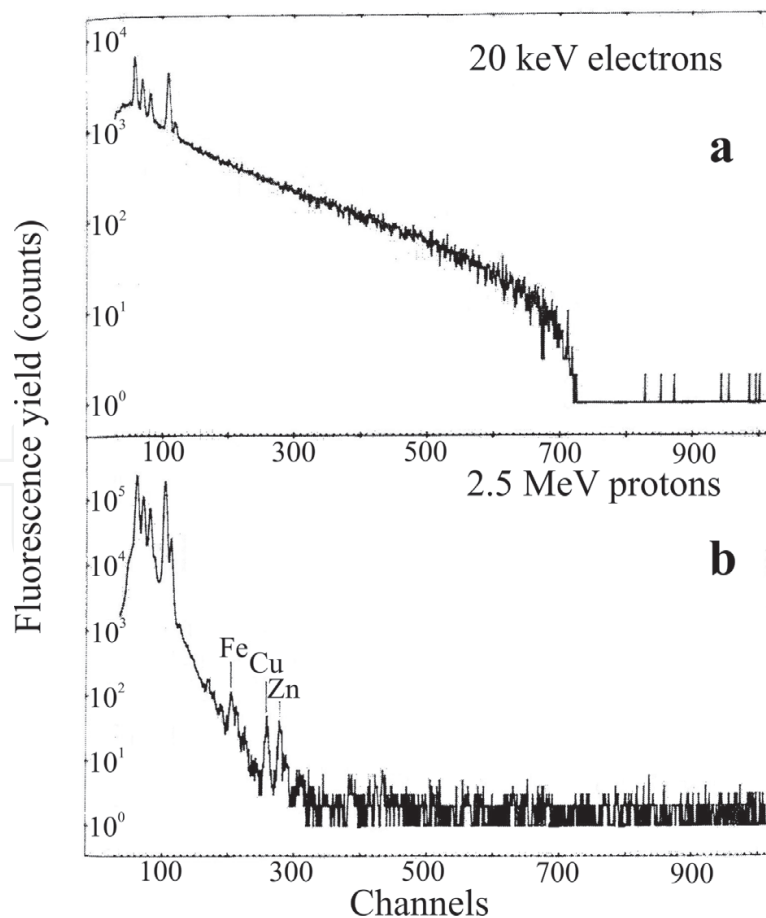

Figure 24. X-ray fluorescence spectra of the human brain tissue collected in conditions of the electron beam (E_0 = 20 keV) excitation (a) and the proton beam (E_0 = 2.5keV)application (b) [36].

comparison shows that the ion beam excitation leads to the background intensity decreasing in result of the bremsstrahlung photon yield reduction. In the presented data, the ion beam excitation application allows to registrate Fe, Cu and Zn atoms presence in the studied target. In the result, one can establish that the PIXE method is characterized by very low magnitudes of detection levels. At the same time, it should be emphasized that the PIXE spectrometry is not the quantitative analytical method. PIXE measurement results are controlled by the matrix effect [37] and by the specific factor connected with the absorption cross-section distinction for different characteristic lines. The last factor is defined by the material layer thickness responsible for the line X-ray fluorescence yield. (This factor can be eliminatedby usingthe planar X-ray waveguide-resonator, see **Figure 5**.)

PIXE element diagnostics, in addition to the matrix and absorption effects, must take into account specific peculiarities of the X-ray fluorescence yield registration by the energy dispersion detector. Any X-ray detector is equipped by the input window, which absorbs the collected radiation. Moreover, X-ray detector is characterized by the reduced efficiency at the high energy photon registration. **Figure 25** presents the experimental diagram reflectingthe X-ray radiation efficiency registration for the wide range of photon energy. Best results of the light element diagnostics can be obtained with X-ray detectors equipped by C_1 and C_2 superfine windows because it allow to collect PIXE spectra up to the photon energy $E \cong 0.1$ keV. As a whole, the PIXE spectrometry is very beautiful supplement to the RBS spectrometry.

4.2. PIXE for the material element analysis

Distinction in the X-ray fluorescence yield excitation cross-section demonstrated in **Figure 23** can be illustrated by the direct experimental measurements. **Figure 26** shows spectra of the
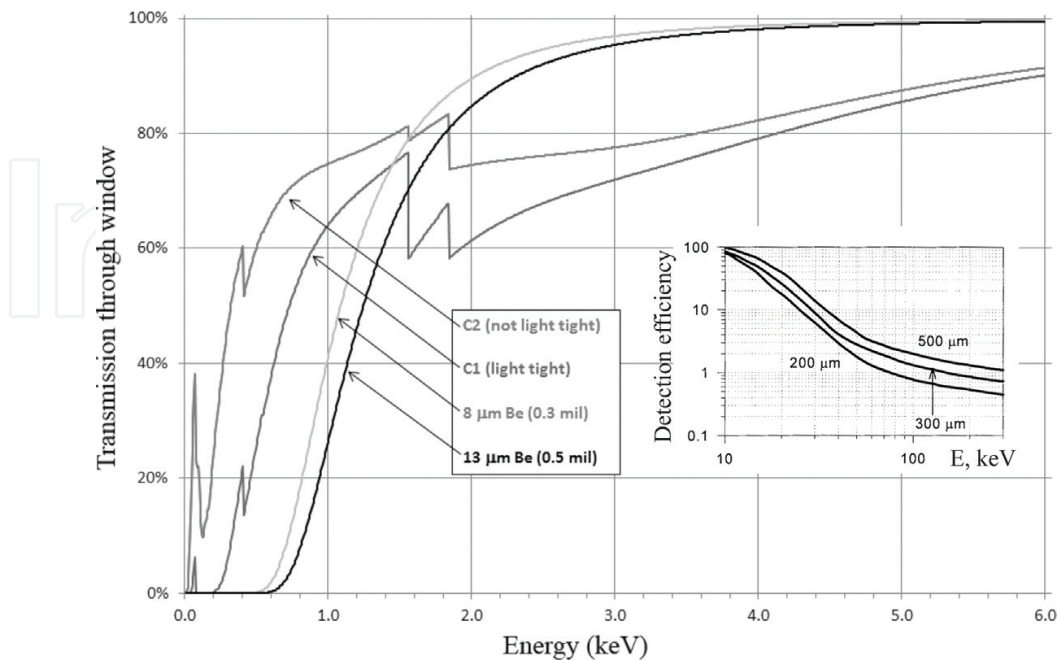

Figure 25. X-ray radiation energy efficiency of the SDD detector equippedby different input windows. Insert shows the efficiency dependence on the detector working plate thickness.
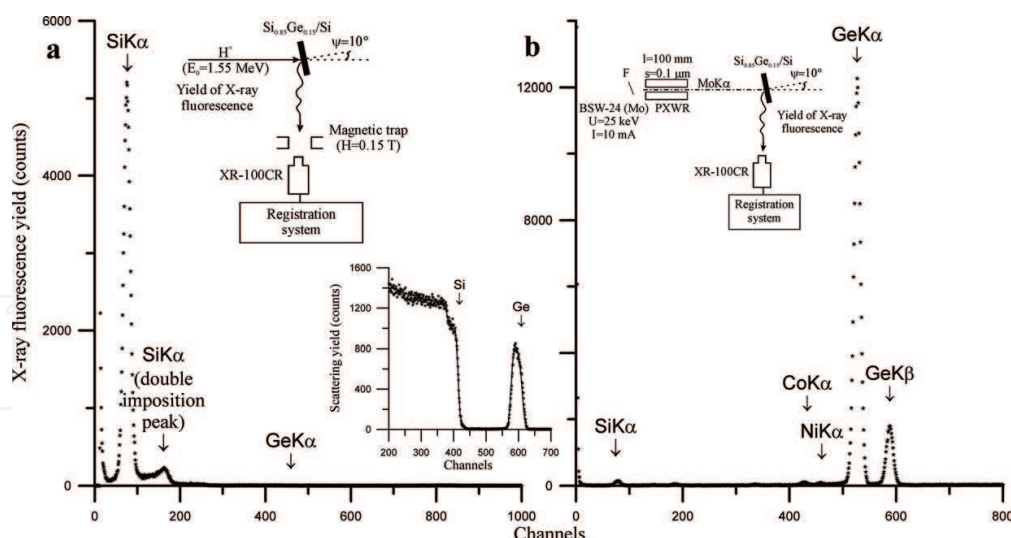
Figure 26. Comparison of X-ray fluorescence yield for $Si_{0.85}Ge_{0.15}$/Si epitaxial structure collected in conditions of the proton beam (a) and the $MoK\alpha$ radiation flux excitation (b). Arrows shows the energy position of X-ray characteristic lines collected by X-ray pin detector. Insertions show the measurements geometry and RBS He^+ ($E_0 = 1.525$ MeV) ions spectrum for the target. Energy steps for ones 1.9 keV/channel.

X-ray fluorescence yield excited by the proton beam and the $MoK\alpha$ radiation flux. For the reference, the figure presents experimental and theoretical RBS spectra of the target. The target is the silicon-germanium epitaxial film with thickness 112 nm on the silicon monocrystal substrate. Experimental spectrum was collected in the target random position. Comparison of X-ray fluorescence spectra collected in conditions of the different excitation methods use shows that the PIXE approach is more effective for the light element diagnostics in materials, but the X-ray fluorescence excitation is more preferable in case of the heavy element analysis. It is very important to notice that the ion beam excitation provokes the X-ray characteristic fluorescence yield by very high intensity. The spectrum excited by the proton beam with current I = 2 nA (1.2×10^{10} ion/sec) was registeredfor 5 seconds, at the same time, the time registration of spectrum excited by the $MoK\alpha$ radiation flux (N = 4×10^5 photon/sec) was equal 300 s. High intensity of the X-ray fluorescence yield characteristic for the first spectrum is borne out by the double imposition peak appearance. So, in the last experiments, we use SDD silicon detector in frame of the Sokol-3 ion beam analytical complex facility, which can work at the enhanced pulse loading without double imposition peaks.

High efficiency of the PIXE light element diagnostics was used in our investigations of the geological object. **Figure 27** shows the proton-induced X-ray emission spectrum of the $(Mg_{0.93}Fe_{0.07})_2SiO_4$ natural olivine. Host composition of the mineral was defined by RBS method. Experimental and theoretical spectra of the object are presented in the figure, too. PIXE measurements allow to fix in the target structure the Ca, Cl, S, Al and Na elements set existence. Quantitative analysis of the target contamination can be carried out by the TXRF spectrometric method [38].

PIXE spectrometry can be used for petroleum contamination analysis. **Figure 28** shows TXRF and PIXE spectra demonstrating the contamination set existence in the petroleum film deposited on Be substrate. RBS spectrum of the film is shown in **Figure 14**. TXRF spectrum allows to
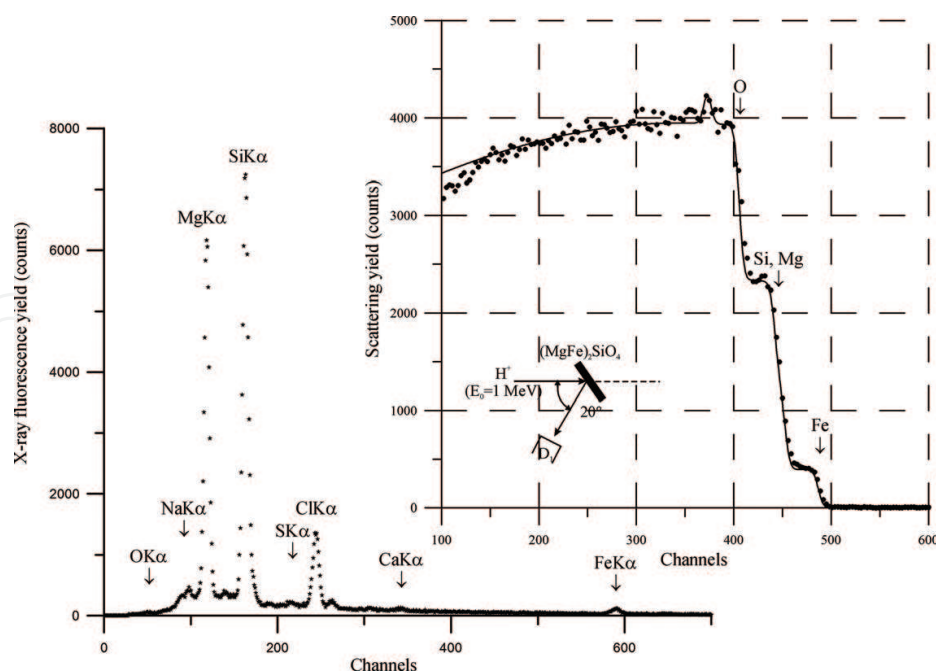
Figure 27. PIXE spectrum of the olivine natural crystal collected in result of H⁺ ion beam excitation. Arrows shows the energy position of X-ray characteristical lines collected by SDD silicon detector. Rutherford backscattering spectrum of the target is presented on insert. Energy step for PIXE spectrum 10.9 eV/channel, for RBS 1.9 keV/channel.

produce the quantitative analysis of the contamination concentration that used the sulfur atomic content as the internal standard. TXRF and PIXE spectra confirm the vanadium atoms presence in the petroleum sample. At the same time, the La atoms concentration diagnostics is inaccessible for the total X-ray external fluorescence spectrometry. PIXE analysis is able to fix the La atoms presence in the petroleum sample. The lanthanum atomic content was evaluated by usingthe comparison method with data for Ca and V atom concentration. It is 0.0005 if the sulfur concentration is elected as a one. PIXE diagnostics of the solution dry residue is the very perspective application for this specific target.

PIXE measurements can be used for the nonstandard element analysis. **Figure 29** shows RBS and PIXE spectra collected for the leather processing material by usingthe proton beam excitation. RBS spectrum allows to evaluate the host elements concentration (except hydrogen atom), at the same time, the PIXE investigation takes possibilities to fix the contamination element presence in the leather processing material. How showed experience of the leather goods manufacturing the chromium and contamination concentrations defines quality of different products manufactured from the leather. The quantitative contamination analysis can be executed by TXRF method application. But if the TXRF spectrometry sensitivity is not enough, it is possible to use the planar X-ray waveguide-resonator for the trace surface element diagnostics in frame of the PIXE excitation of the X-ray fluorescence yield. The experimental scheme for such measurement execution is presented in **Figure 5b**, and the diagnostic method has name – TXRF PE.

Figure 30 presents the experimental data characterizing the method possibilities on base of the old coin study. PIXE spectrum shows X-ray fluorescence lines initiated by surface and
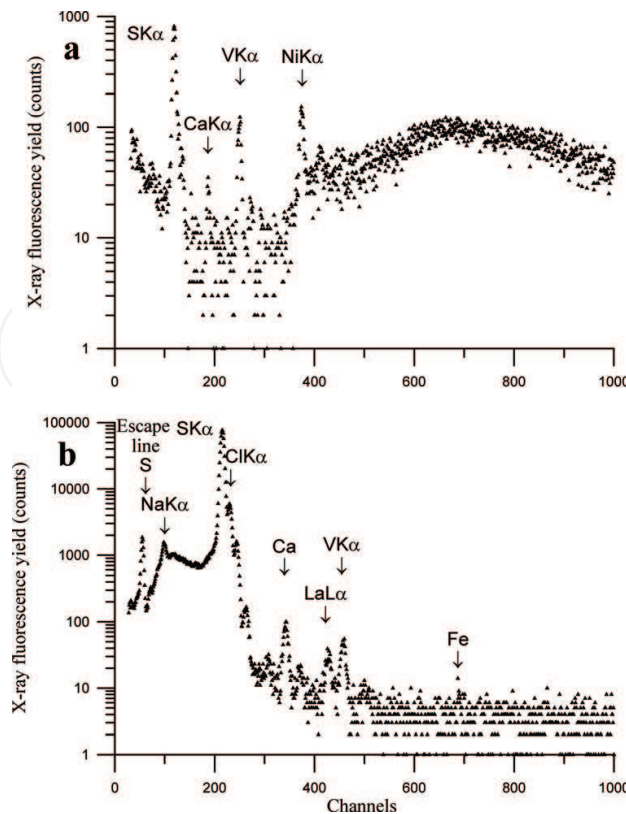
Figure 28. X-ray fluorescence spectra collected for the petroleum film deposited on Be substrate by use the TXRF and the PIXE spectrometry. Energy step for TXRF spectrum 20 eV/channel, and 10 eV/channel for PIXE spectrum. TXRF fluorescence yield was excited by the MoKα flux, PIXE – by the proton beam with energy E_0 = 0.953 MeV. Arrows show the energy position of X-ray characteristic lines collected by SDD silicon detector.
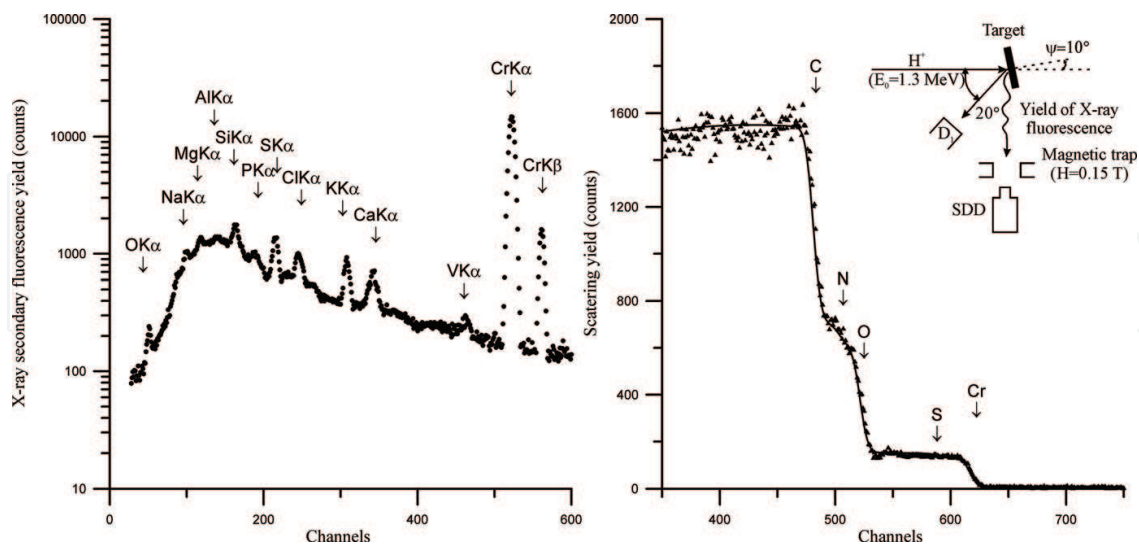
Figure 29. Experimental and theoretical RBS H$^+$ (E_0 = 1.3 MeV) ions for the sample of thin leather – processing material and PIXE spectrum of the one collected in the same experiment. Arrows on the RBS spectrum show the ion scattering energies on nuclei of atoms located on the sample surface, and on the PIXE spectrum show the energy position of X-ray characteristical lines collected by SDD silicon detector. Energy step for RBS spectrum 1.9 keV/channel, for PIXE one 10 eV/channel. Insert shows the measurement geometry.
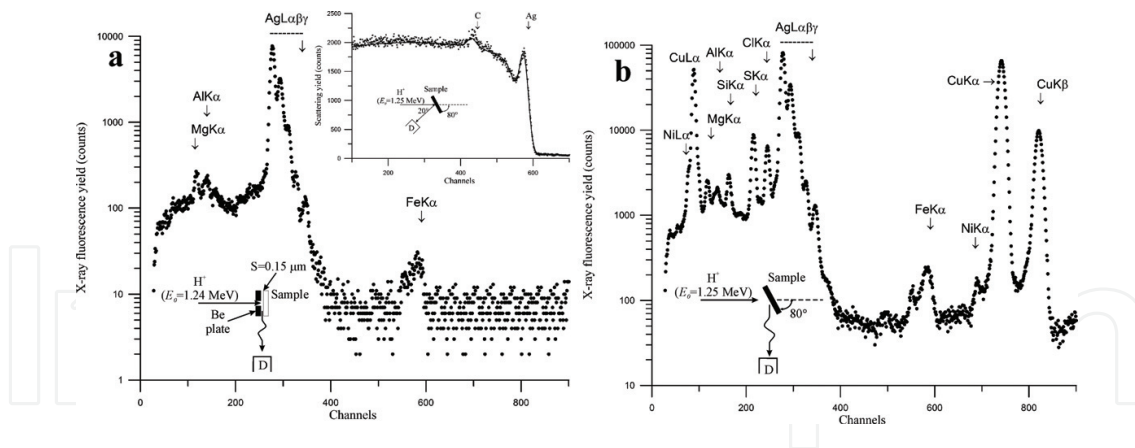
Figure 30. TXRF PE (a) and PIXE (b) spectra of the half copeek old coin fabricated from copper with the surface Ag coating (t= 170 nm) collected by SDD silicon detector in conditions of the X-ray fluorescence excitation by the proton beam (E_0 = 1.25 MeV). Inserts show measurements geometry and RBS H^+ ions spectrum of the target. Arrows on fluorescence spectra show of the energy position of X-ray characteristical lines and on RBS one ion scattering energies on nuclei located on the coin surface. Energy step for fluorescence spectra 10.5 eV/channel for RBS one 1.9 keV/channel.

volume atoms of the target. In its turn, TXRF PE spectrum reflects X-ray fluorescence lines characteristic for the coin surface. (Carbon peak on the Rutherford backscattering diagram is connected with the C-H film appearing in process of the proton beam scattering in the measurement period.) The X-ray fluorescence spectra comparison allows to conclude that the Mg, Al and Fe atoms contamination are typical for the Ag coating. This conclusion was confirmed by the TXRF direct study. So, new experimental method can be recommended for the trace light elements diagnostic in addition to the standard TXRF experimental measurements.

5. Nuclear elastic recoil for the hydrogen diagnostics

It is known, that the hydrogen atoms diagnostic can be carried out by using the direct resonance nuclear reaction, for example,^{1}H(^{15}N; α,γ)^{12}C and ^{1}H(^{19}F; α,γ)^{16}O, or by the nuclear elastic recoil (NER) method [16]. The resonance method has a limited spearing because its application demands ion beams with the enhanced energy. For example, the low energy resonance of ^{1}H(^{15}N; α,γ)^{12}C reaction has value 3.35 MeV. So, the nuclear recoil spectrometry is more accessible while less informative. The experimental scheme for the nuclear recoil method is presented in **Figure 6b**. The measurement scheme assumes the surface target installation on the $\theta_1/2$ small angle about of the helium ion beam propagation line and the recoil and scattering ion detector placing under the θ_1 angle. The detector must have a collimator and the thin film absorber. The absorber thickness must provide a total absorption of the helium ions scattering flux. In these conditions, the recoil hydrogen atoms undergo the noticeable straggling [10–16]. The straggling effect is characterized by the ion beam average energy decreasing attended by increasing of the ΔE energy dispersion. Moreover, it is a need to take into account the adsorbed layer existence on the any material surface, which contains some hydrogen quantity. As a rule, the hydrogen surface concentration is higher in comparison of the hydrogen target volume content.
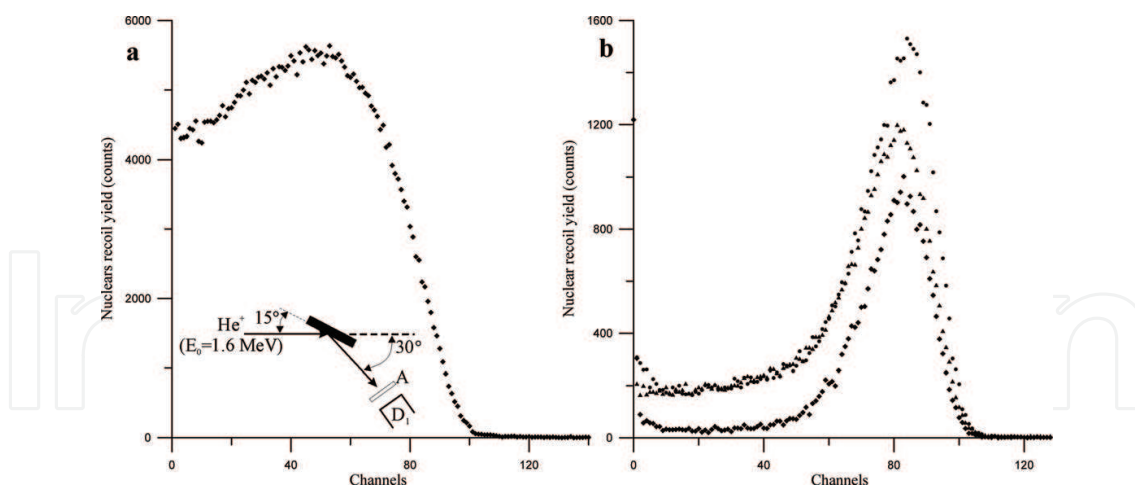
Figure 31. Nuclei elastic recoil spectra of the $TiH_{0.98}$ weighting etalon (a) and some perovskite structures (b) collected in the specific geometry allowed to fix the hydrogen atoms recoil. Hydrogen recoil spectrum for $SrTiO_3$ monocrystal (●), for BSTO film on MgO substrate (▲), for BSTO film Si substrate (♦). Measurement geometry is presented on insert. Energy step 3.8 keV/channel.

The nuclei recoil spectrometry, similar to the RBS method allows to produce the absolute analysis. At the same time, it is possible to use standard samples attested by the precision weighting. We used $TiH_{0.98}$ as the similar etalon. **Figure 31** shows NER spectra of the etalon and some perovskite structures. Data obtained from the etalon spectrum allows to evaluate the hydrogen content in studied perovskite structures. It is very strange but the hydrogen atoms concentration in the $SrTiO_3$ monocrystalline structure was near 4% at. Similar hydrogen content was detected in the BSTO film deposited on MgO substrate. The BSTO film deposited on the silicon substrate had smaller hydrogen atoms in its structure (near 1% at.). Evaluation of the hydrogen atoms in surface absorbed layers shows that the film has the C_1H_1 composition. NER measurements are characterized by specific conditions. The helium ion beam energy must be higher as 1.5 MeV. At smaller energy of the beam some experimental and interpreting difficulties appear.

6. Nuclear reaction analysis application for the material study

Nuclear reactions excited by high energy ion beams can have the resonance nature and can demonstrate the threshold characteristics[39]. It is the isotopically sensitive methods. Some nuclear reactions have the practical significance. It is the $^{27}Al(p,\gamma)^{28}Si$ famous resonance reaction, which uses for the ion beam accelerator calibration [40]. Nuclear reaction analysis (NRA) is mostly used for the light element diagnostics in material. In our work we applied the $^{11}B(p,\alpha)^8Be$ nuclear reaction for study of the electro-rocket engine function peculiarities [41]. The main investigation task of the study was the elements spatial distribution determination in the engine output jet. The engine discharge chamber was manufactured from the material elaborated on the BN base composition. So, it is expected that the main admixture element in the xenon jet will be boron. For the boron spatial distribution in the engine jet, we used the Be plates set arranged on different angles about the jet propagation line. The deposit on the Be
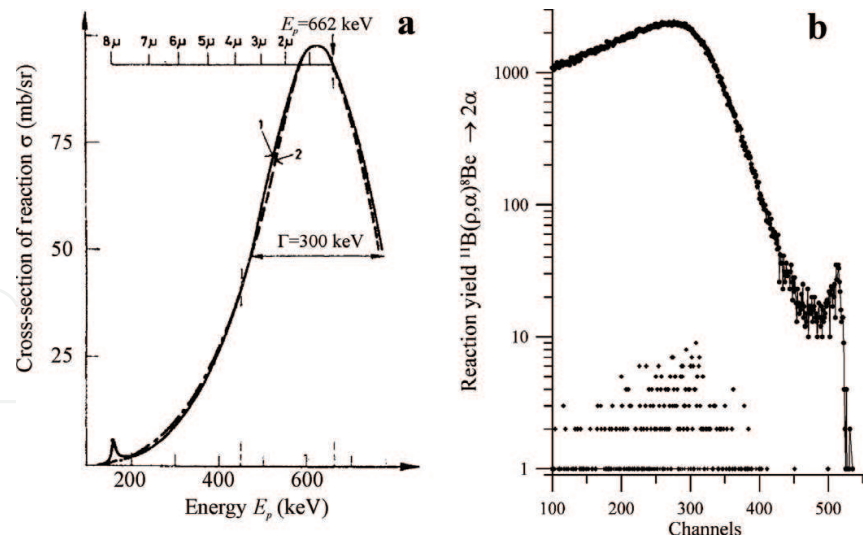
Figure 32. Cross-section energy dependence of the ^{11}B(p, α)^{8}Be nuclear reaction (a) [43], and the reaction yields for the $B_{0.4}N_{0.45}X_{0.15}$ engine ceramic, for the Be plate with deposited film, which was arrangement on angle 59 about the jet propagation line and for the Be clean plate.

Isotope	Content in nature, %	Nuclear reaction	Energy of proton, keV	Cross-section of reaction, mb/sr	Width of resonance, keV	Emission product E_γ, E_α, MeV	Limits detection, at.%
^{6}Li	7.62	—	—	—	—	—	—
^{7}Li	92.58	^{7}Li(p.γ)Be^8	441	6	12	17.65; 14.75	~100 ppm
^{9}Be	100	^{9}Be(p,α)^{6}Li	330	4	1.5	8.5; 14.2	~50 ppm
^{10}B	19.61	^{10}B(p,γ)	1146	0.01	570		~10 ppm
^{11}B	80.39	^{11}B(p,α)^{8}Be	650	90	10	-; 3.7	~10 ppm
^{12}C	98.89	^{12}C(p,γ)^{13}N	459	0.13	40	2.36; —	~120 ppm
^{13}C	1.11	^{13}C(p,γ)^{14}N	550	1.44	32	8.6; —	~100 ppm
^{14}N	99.64	^{14}N(p,γ)^{15}O	278	~0.01	1.6	6.8	~100 ppm
^{15}N	0.36	^{15}N(p,γ)^{12}C	898	800	2.2	4.43	~10 ppm
^{16}O	99.8	—	—	—	—	—	—
^{18}O	0.2	^{18}O(p,α)^{15}N	730	15	10	3.4	~10 ppm
^{19}F	100	^{19}F(p,γ,α)^{16}O	872	661	4.5	6.13	~1 ppm
^{23}Na	100	^{23}Na(p,α)^{20}Ne	592	4	45	2.238	~20 ppm
^{24}Mg	78.6	^{24}Mg(p,γ)Al^{25}	1200	~0.01	<10	3.44; 1.83; 1.61	~200 ppm
^{25}Mg	10.2	^{25}Mg(p,γ)Al^{26}	317	~0.01	12	6.19; 4.86; 0.82	~500 ppm
^{26}Mg	11.2	^{26}Mg(p,γ)Al^{25}	661	~0.01	<10	7.88; 6.68; 5.9	~500 ppm
^{27}Al	100	^{27}Al(p,γ)^{28}Si	992	0.1	0.05	1.77; 7.93; 10.78	~10 ppm

Table 1. Resonant nuclear reaction parameters for light element isotopes initiated by proton beams.

plates was analyzed by the boron resonance reaction. Cross-section energy dependence of the reaction is presented in **Figure 32a** [42]. **Figure 32b** shows the pattern of our measurements, which allowed to evaluate the boron spatial distribution in the jet of electro-rocket engine. Similar investigations are very effective but are very expensive. At the same time, it is useful to have a grasp about possibilities of NRA methods application and atomic detection limits determination on base of the real nuclear reaction use. **Table 1** presents the information about the most useful reaction applied for the light element diagnostics.

7. Some peculiarities of the ion beam optical luminescence excitation

Our active investigations in the optical scintillation field at ion beam excitation were connected with the $PbWO_4$ and LaF_3 luminescence response study [43–45]. Interest to the $PbWO_4$ luminescence characteristic study was initiated by the fast component existence in the luminescence response at the proton beam excitation. There was the specific interest to fix the luminescence distinction between yields in the random and the channeling orientation of the crystal and to study kinetic of the luminescence yield dependence on the absorbed radiation doze. Results of these investigations are shown partially of **Figure 33**. The luminescence spectrum obtained in the channeling proton beam condition demonstrates some integral intensity yield increasing [43] and is characterized by some spectrum variation. Dosimetric data showed that luminescence yield intensity reduces as the radiation doze increases up to some critical value J_∞. After
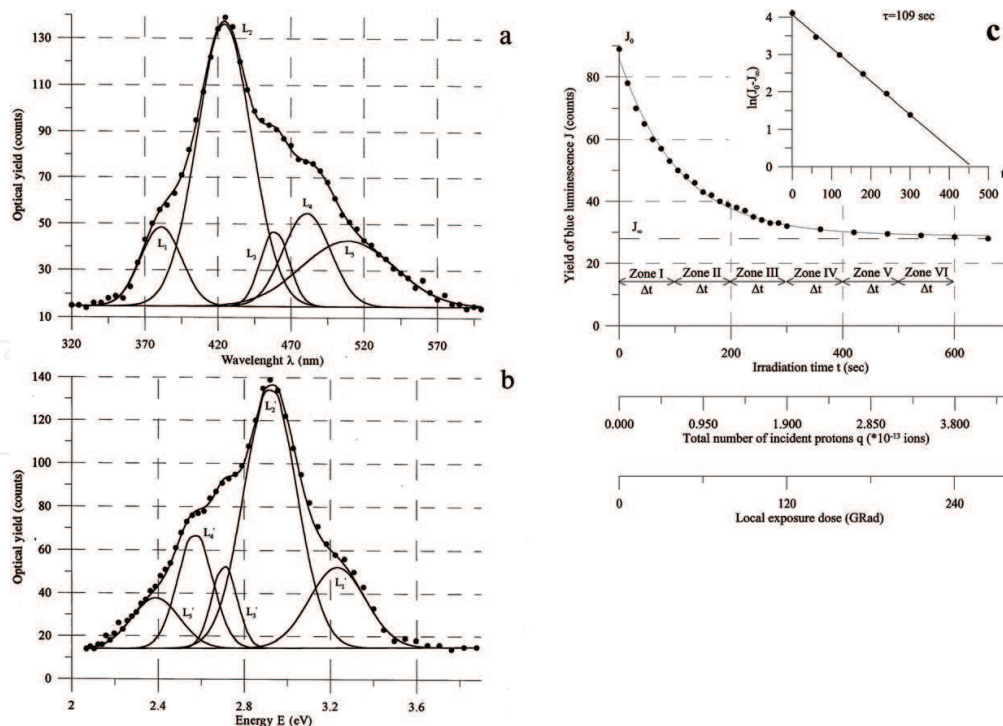

Figure 33. Luminescence yield optical spectra for random (a) and channeling along [001] axis (b) of $PbWO_4$ monocrystal target executed by H^+ ions beam ($E_0 = 0.9$ MeV), and the kinetic function of random spectrum blue component ($\lambda_0 = 412$ nm) on the absorbed radiation dose.

warning at t = 100°C during τ=600 s, the PbWO$_4$ target had got the critical radiation doze returned into the initial state. Total interpretation of the experimental data is very difficult, but some results of our investigations were found useful for the elaboration of the PbWO$_4$ mono-crystal great size preparation technology. The experimental arrangement used for our luminescence study in conditions of the ion beam excitation is presented in **Figure 6**. The ion luminescence investigations does not have wide spread use owing to the interpretation problems existence. At the same time, it is a need to understand that the ion beam luminescence excitation mechanism is different from the X-ray, gamma ray and electron beam excitation one. In case of the PbWO$_4$ excitation by the proton beam, we can observe the L$_1$ luminescence line being absent at any other excitation types.

8. Monocrystalline and epitaxial structures study by the ion beam channeling method

How it was discussed early peculiarities of the ion beams interaction with materials is defined by the material structure features. Experimental investigations of very much crystals confirmed the Starks assumption about possibility for high energy ions to propagate through the crystal almost without scattering in case of its movement along ordered atomic chains [46]. This effect was called the ion beam channeling in crystals. Fundamental features of the effect and its possible practical application were discussed in details in the specific monograph [20]. Some features of the effect were studied in our investigation. **Figure 34** shows this effect observation for the monocrystalline synthetic diamond target prepared by the temperature gradient method realized at the high hydrostatic pressure conditions. Ion beams axial channeling along [100] axis of the target demonstrates the high perfection structure (χ_{exp} = 0.23 at χ_{tcor} = 0.09). W atoms are the main admixture of the target. The hydrogen ion channeling allows to evaluate the channeling effect depth for the diamond. SiO$_2$ thin film presents on the diamond surface. It is the result of polishing procedure. The studied diamond target has noticeable sizes (0.5 × 5 × 5 mm^3). It can be used as the substrate for the power integral circuits
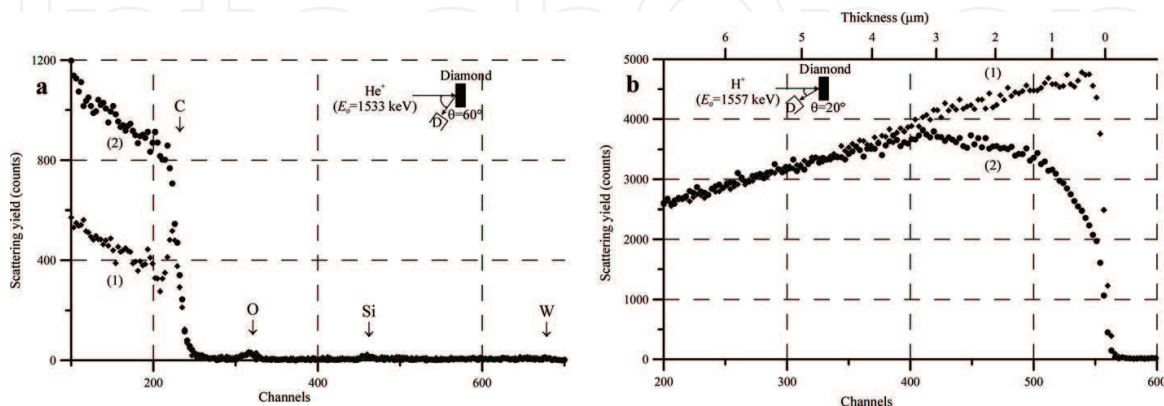

Figure 34. Experimental RBS He$^+$ and H$^+$ ions spectra for the random position (a) and the channeling orientation through [100] axis (b) of the diamond monocrystal. Arrows show the ion scattering energies on nuclei of atoms located on the target surface. Measurement geometries are shown on inserts. Energy step 1.9 keV/channel. (1) Random orientation. (2) Channeling.
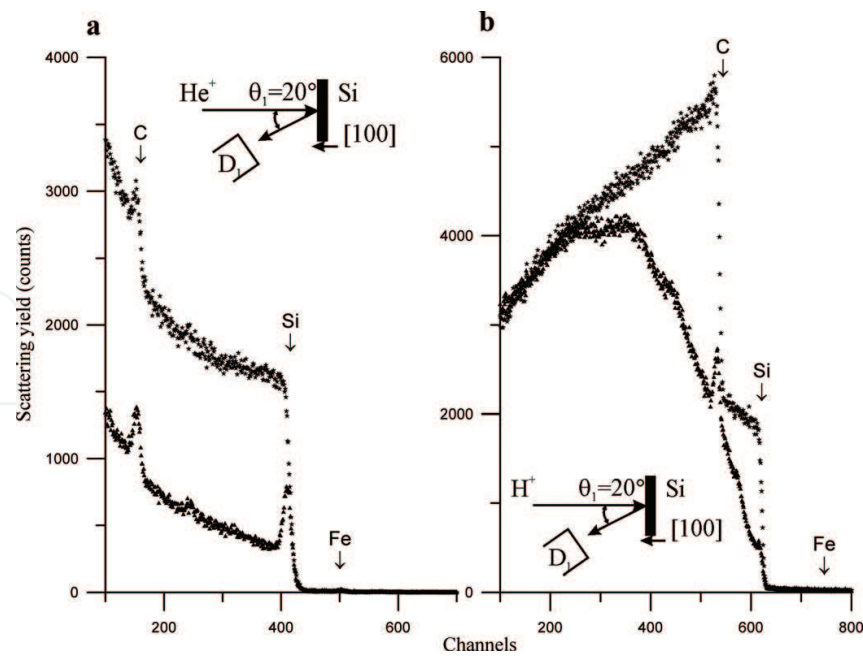
Figure 35. Experimental RBS He$^+$(a) and H$^+$(b) ions spectra for theSiCmonocrystal in the random position and the channeling condition along [001] axis. Arrows show the ion scattering energies on nuclei of atoms located on the target surface. Experimental geometries is shown on inserts. Energy step 1.9 keV/channel.

preparation and the X-ray tube windows manufacturing owing to its high thermal conductivity. Other sample of the ion beams axial channeling is shown in **Figure 35**. It demonstrates patterns of He$^+$ and H$^+$ ion beams channeling along [001] axis of SiC monocrystal prepared by the Lely method [47]. RBS measurements executed for the random and oriented conditions showed that the silicon carbide crystalline structure has high perfection (χ = 0.36). The target structure is characterized by the 6H hexagonal polytype with crystallographic parameters of the cell a = 0.308 nm, c = 1.512 nm. Because the preparation method is connected with molten metals, Fe atoms are a chief contamination of the target. The technology preparation of SiC monocrystalline boules is very important for the nanophotonics because the silicon carbide material is very suitable for manufacture of light emitting diodes (LED) on base of the high energy-gap semiconductors. In the context of this, very interesting works of Prof. Kukushkin are connected with combination of the silicon and the silicon carbide technologies [48]. He elaborated the technology of SiC/Si epitaxial heterostructure preparation. The ion beam analysis application showed that the SiC/Si heterostructure is characterized by low perfection but the crystallographic epitaxy existence [49]. Moreover, on base of the SiC/Si substrate,they were able to prepare the effective light emission structure. So, the ion beam analysis application to the compositions diagnostics having the SiC structure has the direct practical application.

The living practical interest is connected with perovkite crystals and its heterostructures investigations. It is well known, that multielement oxide films fabricated on base of the doped barium titanate (BaTiO$_3$) are assumed to be promising material structures for the development of micro and nanoelectronic and electro-optical devices. Such coatings are potentially applicable as electro-optical modulators and phase shifter, switching devices, optical microprocessors, surface waveguide-acoustic transducers and capacitive elements in dynamic memory. Experimental investigations showed that the epitaxial coatings on single crystals substrates with appropriate
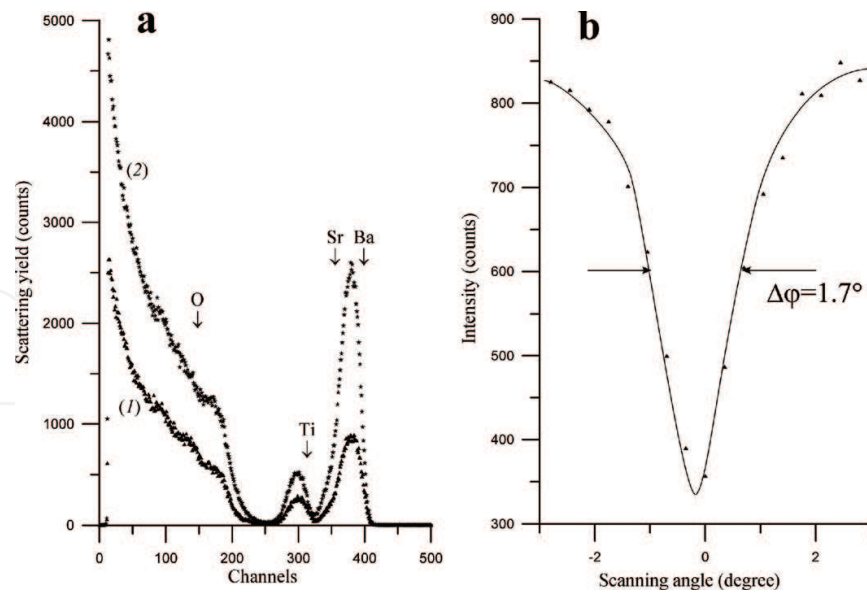
Figure 36. Experimental RBS He$^+$ions spectra for Ba$_{0.8}$Sr$_{0.2}$TiO$_3$/MgO epitaxial structure in the random position and the channeling condition along [100] structure axis (a) and the rocking resette near the channeling axis (b). Arrows show the ion scattering energies on nuclei of atoms located on the target surface. Measurement geometry is presented on the insert. Energy step 1.9 keV/channel.

crystallographic parameters exhibit the best electro-optical properties. So, the BSTO films study deposited on different substrates were one of our priority films study deposited on research direction. **Figure 36** shows experimental RBS spectra of the Ba$_{0.8}$Sr$_{0.2}$TiO$_3$/MgO epitaxial heterostructure collected for the target random position and in conditions of He$^+$ ion beam channeling along [100] direction. Comparison of He$^+$ ion scattering spectra collected in the random and channeling target disposition shows that the scattering yield proportional decreasing for the film and substrate atoms takes place. Moreover, rocking rosettes obtained for film and substrate atoms showed the identical form. At the same time, it is a need to notice that the χ experimental factor for the target is twice as much as the theoretical magnitude χ_{min} = 0.18. It is showed that the target structure is characterized by some nonperfection. But the ion beam channeling along the sole crystallographic axis does not always reflect real degree of the target structure perfection. Similar information can be accessible at the channeling data use for some crystallographic axis. Sample of such situation is presented in **Figure 37**. It shows experimental and theoretical RBS He$^+$ ions spectra for the Si$_{0.8}$Ge$_{0.2}$/Si epitaxial structure obtained for random target positions and oriented states and the rocking rosettes of the ion beam channeling near [100] and [110] axis [50]. The minimum yield for the He$^+$ ion beam channeling along [100] axis is near this parameter theoretical magnitude (χ_{min} = 0.03). One can expect on base of the RBS channeling spectrum that the thin film epitaxial structure is characterized by the almost ideal perfection. But the ion beam channeling spectrum along [110] crystallographic axis does not confirm the similar expectation. Experimental magnitude of the minimum yield parameter for the [110] silicon crystallographic axis is higher as the theoretical one on two times. This discrepancy is connected with the elastic stress owing to the magnitudes difference of film and substrate unit cells. In this case, the structure distortions have an anisotropic character. The stress value is dependent on the film composition and its thickness. Thick films demonstrate the exfoliation trend. The channeling method can be used with success for the light element diagnostic
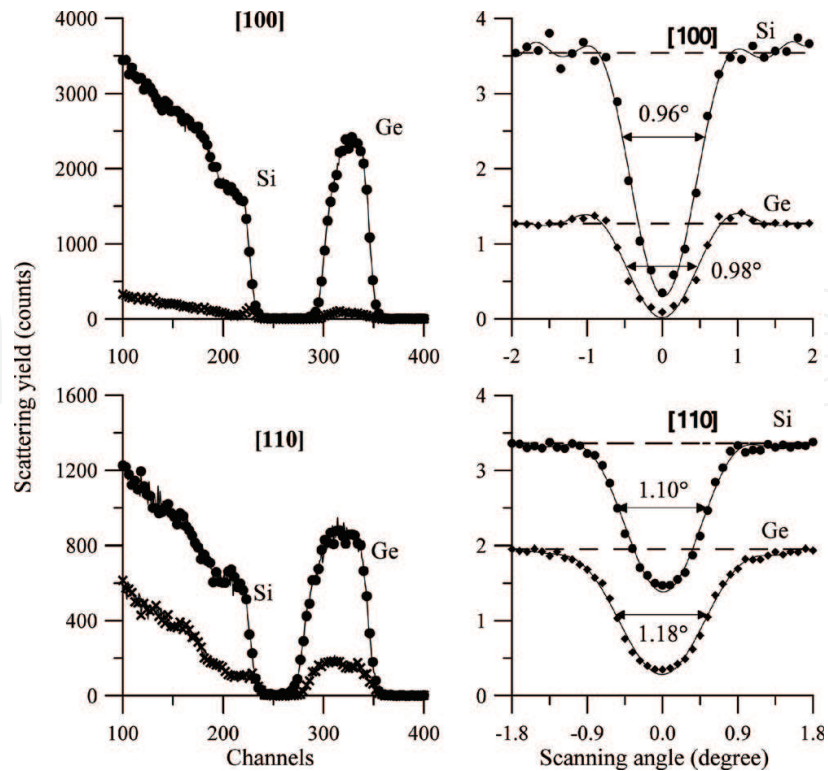
Figure 37. Experimental RBS He$^+$ions spectra for $Si_{0.8}Ge_{0.2}$/Si epitaxial structure in the random positions and the channeling conditions along [100] axis, [110] axis and the rocking rosettes near the channeling axis. Arrows show the ion scattering energies on nuclei of atoms located on the target surface. Measurement geometries is shown on inserts. Energy step 1.9 keV/channel.

implanted into the monocrystalline objects. It has possibilities to study the structure defects types and its distribution [22]. But it is a need to notice that the channeling method is very expencive.

9. Conclusion

Short review of the ion beam spectrometry and analytical method built on base of the ion beams interaction with material shows that the methods application is very useful and in some cases unique. All ion beam analytical methods are the nondestructive technique. RBS spectrometry is the only instrumental method being not demanded analytical standards and etalons. Complex application of the material ion beam analysis allows to present the total description of the material properties. But the cost of its use is very high.

Acknowledgements

competitiveness of Peoples' Friendship University of Russia (RUDN University) among the world's leading research and education centers in the 2016–2020.

Author details

Vladimir Egorov[1]* and Evgeny Egorov[1,2]

*Address all correspondence to: egorov@iptm.ru

1 Institute of Microelectronics Technology Russian Academy of Science (IMT RAS), Chernogolovka, Russia

2 RUDN University, Moscow, Russia

References

[1] Schmidt B, Wetzig K. Ion Beam in Material Processing and Analysis. Wien: Springer; 2013. p. 418

[2] Bird JR, Williams JS. Ion Beams for Material Analysis. Sidney: Academic Press; 1989. p. 719

[3] Townsend PD. Optical effect of ion implantation. Reports on Progress in Physics. 1987;**50**: 501-558

[4] Pop SS, Belikh SF, Drobnich VG, Ferleger VK. Ion-Photon Metal Emission. Tashkent: FAN; 2000. p. 200 (In Russian)

[5] Huddle JR, Grant PG, Ludington AR, Foster RL. Ion beam-induced luminescence. NIM. 2007;**261**:475-476

[6] Koljada VM, Zaychenko AK, Dmitrenko PV. X-Ray Spectral Analysis at the Ion Beam Excitation. Moscow: Atomizdat; 1978. p. 248 (In Russian)

[7] Johansson SAE, Campbell JL. PIXE: A Novel Technique for Element Analysis. New York: Wiley; 1988. p. 347

[8] Instrumentation for PIXE and RBS. Special Issue of International Atomic Energy Agency (IAEA). IAEA-TECDOC-1190. Vienna: IAEA; 2000. p. 83

[9] Petrov NN, Abrojan IA. Surface Diagnostics by Ion Beams Application. Leningrad: LGU Press; 1977. p. 160 (In Russian)

[10] Chu WK, Majer JM, Nicolet MA. Backscattering Spectrometry. New York: Academic Press; 1978. p. 384

[11] Shipatov ET. Background Scattering of Fast Ions, Theory, Experiment, Practice. Rostov-on-Don: Rostov State Univ. Press; 1988. p. 155

[12] Tesmer JR, Nastasi M, editors. Handbook of Modern Ion Beam Material Analysis. Pittsburg: MRS Published; 1995. p. 704

[13] Hellbord J, Whitlow HJ, Zhang Y. Ion Beams in Nanosize and Nanotechnology. Heidelberg: Springer; 2009. p. 457

[14] Nastasi M, Mayer JW, Wang Y. Ion Beam Analysis, Fundaments and Application. Boca Raton: CRC Press; 2015. p. 434

[15] Chernov IP, Shadrin VN. Analysis of Hydrogen and Helium Concentration by the Nuclei Recoil Method. Moscow: Energoatomizdat; 1988. p. 129 (In Russian)

[16] Hofsas H. Forward Recoil Spectrometry. New York: Plenum; 1996. p. 278

[17] Amsel G, Lanford WA. Nuclear reaction techniques in material analysis. Annual Review of Nuclear and Particle Science. 1984;**34**:435-460

[18] Ehmann WD, Vance DE. Radiochemical and Nuclear Methods of Analysis. New York: Wiley; 1991. p. 531

[19] Rauhala E. Proton elastic scattering cross-section of carbon, nitrogen and silicon for backscattering analysis in the energy range 0.7-2.5 MeV. NIM. 1985;**12**:447-452

[20] Feldman LC, Mayer JW, Picraux ST. Material Analysis by Ion Channeling. New York: Academic Press; 1982. p. 300

[21] Shipatov ET. Ions Channeling. Rostov-on-Don: Rostov State Univ. Press; 1986. p. 144 (In Russian)

[22] Gotz G, Gartner K, editors. High Energy Ion Beam Analysis of Solids. Berlin: Acad. Verlag; 1988. p. 342

[23] Doolittle LR. Algorithm for the rapid simulation of Rutherford backscattering spectra. NIM. 1985;**9**:344-351

[24] Egorov V, Egorov E, Afanas'ev M. TXRF spectrometry at ion beam excitation. IOP Publishing; IOP Conf. Ser.: Journal of Physics: Conf. Ser. 2017;**808**:012002. DOI:10.1088/1742-6596/808/1/012002

[25] Egorov V, Egorov E. Waveguide-resonance mechanism for X-ray beam propagation. Advances of X-ray Analysis. 2003;**46**:307-315

[26] Zieglar JF. The Stopping and Ranges of Ions in the Matter. New York: Pergamon Press; 1977. p. 367

[27] Mayer M. SIMNRA: simulation of RBS, ERD and NRA spectra [Internet]. 1999. Available from: http://home.mpcdf.mpg.de/~mam/Mayer-AIP-Conference-Proceedings-475-(1999)-541.pdf [Accessed: 2018–02-19]

[28] Mehrer H. Diffusion Is Solids, Fundaments, Methods, Materials, Diffusion-Controlled Processes. Berlin: Springer; 2007. p. 651

[29] Poate M, Tu KN, Mayer JW, editors. Thin Film Interdiffusion and Reactions. New York: Wiley; 1978. p. 578

[30] Aleshin AN, Egorov VK, Bokstein BS, Kurkin PV. Study of diffusion in thin au/cu films. Thin Solid Films. 1993;**223**:51-55

[31] Aleshin AN, Bokstein BS, Egorov VK, Kurkin PV. Segregation effect on grain-boundary diffusion in thin metallic films. Thin Solid Films. 1996;**275**:144-147

[32] Egorov VK, Kononenko OV, Kondratiev OS. Porosity of film coatings in Rutherford backscattering. Surface Investigation. 1988;**13**:729-741

[33] Natelson D. Nanostructures and Nanotechnology. Cambridge: Cambridge Univ. Press; 2015. p. 630

[34] Cahill TA. Proton microprobs and partical induced X-ray analytical system. Annual Review of Nuclear and Particle Science. 1980;**30**:211-252

[35] Folkman F, Gaarde G, Huus T, Kemp K. Proton induced X-ray emission as a tools for trace element analysis. NIM. 1974;**116**:487-499

[36] Johanson SAE, Campbell JL, Malquist KG. Particle Induced X-Ray Emission Spectrometer (PIXE). New York: Wiley; 1995. p. 451

[37] Seppala A, Raisanen J. Matrix effects in particle induced X-ray emission channeling measurements of ZnSe/GaAs heterostructures. Applied Physics Letters. 1999;**75**(6):820-822

[38] Klockenkamper R. Total Reflection X-Ray Fluorescence Analysis. New York: Wiley; 1997. p. 245

[39] Verma HR. Atomic and Nuclear Analytical Methods. Berlin: Springer; 2007. p. 375

[40] Scharf VH. Particle Accelerators Application in Technology and Research. Somernet: Res. Stud. Press; 1989. p. 663

[41] Arbatskii VM, Nadiradze AB, Chirov AA, Shaposhnikov VV, Egorov VK. The study of the angular distribution of doped elemental composition in a jet of an electro-rocket engine by ion beam methods. Surface Investigation. 2001;**16**:875-888

[42] Golicheff I, Locullet M, Engelman C. Analytical application of the direct observation of nuclear reactions induced by low energy protons and leading to the emission of gamma-photons which are measured. Journal of Radioanalytical Chemistry. 1972;**12**:233-250

[43] Egorov VK, Zuev AP, Egorov EV. Scintillation response of monocrystal $PbWO_4$ to random and channeled ions. NIM. 1996;**119**:418-424

[44] Egorov V, Zuev A, Egorov E. Light output of scintillation upon ion excitation of surface layers of $PbWO_4$ single crystal in oriented and nonoriented positions. Surface Investigation. 1997;**12**:717-731

[45] Egorov VK, Egorov EV. Luminescence kinetics of $PbWO_4$ crystal at excitation by H^+ ion beam. NIM. 2001;**179**:536-542

[46] Stark J. Bemerkung uber strahlen zerstreuung und absorption von beta strahlen und rontgenstrahlem in kristallen. Physikalishce Zeitschrift. 1912;**13**:973-988

[47] Lely JA. Darstellung von einkristallen von silicium carbide und beherrschung von art und menge der eingebauten verunreinigungen. Berichte der Deutschen Keramischen Gesellschaft. 1955;**32**:226-264

[48] Kukushkin SA, Osipov AV. New method for growing silicon carbide on silicon by solid phase epitaxy, model and experiment. Physics of the Solid State. 2008;**50**(7):1238-1245

[49] Egorov VK, Egorov EV, Kukushkin SA, Osipov AV. Structural heteroepitaxy during thermochemical transformation of silicon to silicon carbide. Physics of the Solid State. 2017;**59**:135-141

[50] Vyatkin AF, Egorov VK, Egorov EV. Study of strain relaxation in epitaxial structure $Ge_{0.2}Si_{0.8}$/Si at thermo-implantation treatment by ion beam channeling. Materials Research Society Symposium Proceedings. 2000;**585**:183-189